

1 LEVERAGING MULTI-MESSENGER ASTROPHYSICS FOR DARK MATTER SEARCHES

By

Daniel Nicholas Salazar-Gallegos

A DISSERTATION

Submitted to
Michigan State University
in partial fulfillment of the requirements
for the degree of

Physics—Doctor of Philosophy
Computational Mathematics in Science and Engineering—Dual Major

Today

ABSTRACT

3 I did Dark Matter with HAWC and IceCube. I also used Graph Neural Networks

⁴ Copyright by

⁵ DANIEL NICHOLAS SALAZAR-GALLEGOS

⁶ Today

ACKNOWLEDGMENTS

8 I love my friends. Thanks to everyone that helped me figure this out. Amazing thanks to the people
9 at LANL who supported me. Eames, etc Dinner Parties Jenny and her child Kaydince Kirsten, Pat,
10 Andrea Family. You're so far but so critical to my formation. Unconditional love. Roommate

TABLE OF CONTENTS

| | | |
|----|--|------|
| 12 | LIST OF TABLES | vii |
| 13 | LIST OF FIGURES | viii |
| 14 | LIST OF ABBREVIATIONS | xi |
| 15 | CHAPTER 1 INTRODUCTION | 1 |
| 16 | CHAPTER 2 DARK MATTER IN THE COSMOS | 2 |
| 17 | 2.1 Introduction | 2 |
| 18 | 2.2 Dark Matter Basics | 3 |
| 19 | 2.3 Evidence for Dark Matter | 4 |
| 20 | 2.4 Searching for Dark Matter: Particle DM | 11 |
| 21 | 2.5 Sources for Indirect Dark Matter Searches | 16 |
| 22 | 2.6 Multi-Messenger Dark Matter | 18 |
| 23 | CHAPTER 3 MULTIMESSENGER ASTROPHYSICS: DETECTING HIGH EN- | |
| 24 | ERGY NEUTRAL MESSENGERS | 21 |
| 25 | 3.1 Introduction | 21 |
| 26 | 3.2 Charged Particles in a Medium | 21 |
| 27 | 3.3 Photons (γ) | 22 |
| 28 | 3.4 Neutrinos (ν) | 22 |
| 29 | 3.5 Opportunities to Combine for Dark Matter | 22 |
| 30 | CHAPTER 4 HIGH ALTITUDE WATER CHERENKOV (HAWC) OBSERVATORY . | 24 |
| 31 | 4.1 The Detector | 24 |
| 32 | 4.2 Events Reconstruction and Data Acquisition | 24 |
| 33 | 4.3 Remote Monitoring | 24 |
| 34 | CHAPTER 5 ICECUBE NEUTRINO OBSERVATORY | 25 |
| 35 | 5.1 The Detector | 25 |
| 36 | 5.2 Events Reconstruction and Data Acquisition | 25 |
| 37 | 5.3 Northern Test Site | 25 |
| 38 | CHAPTER 6 COMPUTATIONAL TECHNIQUES IN PARTICLE ASTROPHYSICS . | 26 |
| 39 | 6.1 Neural Networks for Gamma/Hadron Separation | 26 |
| 40 | 6.2 Parallel Computing for Dark Matter Analyses | 26 |
| 41 | CHAPTER 7 GLORY DUCK | 27 |
| 42 | 7.1 Dataset and Background | 27 |
| 43 | 7.2 Analysis | 29 |
| 44 | 7.3 HAWC Results | 34 |
| 45 | 7.4 Glory Duck Combined Results | 35 |
| 46 | CHAPTER 8 NU DUCK | 42 |

| | | |
|----|------------------------|----|
| 47 | BIBLIOGRAPHY | 43 |
|----|------------------------|----|

LIST OF TABLES

| | |
|--|----|
| <p>49 Table 7.1 Summary of the relevant properties of the dSphs used in the present work. 50 Column 1 lists the dSphs. Columns 2 and 3 present their heliocentric distance 51 and galactic coordinates, respectively. Columns 4 and 5 report the J-factors of 52 each source given from the \mathcal{GS} and \mathcal{B} independent studies and their estimated 53 $\pm 1\sigma$ uncertainties. The values $\log_{10} J$ (\mathcal{GS} set) [30] correspond to the mean 54 J-factor values for a source extension truncated at the outermost observed star. 55 The values $\log_{10} J$ (\mathcal{B} set) [31] are provided for a source extension at the tidal 56 radius of each dSph. Bolded sources are within HAWC's field of view and 57 provided to the Glory Duck analysis.</p> | 31 |
| <p>58 Table 7.2 Summary of dSph observations by each experiment used in this work. A 59 ‘-’ indicates the experiment did not observe the dSph for this study. For 60 Fermi-LAT, the exposure at 1 GeV is given. For HAWC, $\Delta\theta$ is the absolute 61 difference between the source declination and HAWC latitude. HAWC is more 62 sensitive to sources with smaller $\Delta\theta$. For IACTs, we show the zenith angle 63 range, the total exposure, the energy range, the angular radius θ of the signal or 64 ON region, the ratio of exposures between the background-control (OFF) and 65 signal (ON) regions (τ), and the significance of gamma-ray excess in standard 66 deviations, σ.</p> | 32 |
| <p>67 Proof I know how to include</p> | |

LIST OF FIGURES

| | | | |
|----|------------|---|----|
| 69 | Figure 2.1 | Rotation curve fit to NGC 6503 from [7]. Dashed line is the contribution 70 from visible matter. Dotted curves are from gas. Dash-dot curves are from 71 dark matter (DM). Solid line is the composite contribution from all matter 72 and DM sources. Data are indicated with bold dots with error bars. Data 73 agree strongly with a matter + DM composite prediction. | 5 |
| 74 | Figure 2.2 | Light from distant galaxy is bent in unique ways depending on the distribution 75 of mass between the galaxy and Earth. Yellow dashed lines indicate where 76 the light would have gone if the matter were not present [8]. | 7 |
| 77 | Figure 2.3 | (left) Optical image of galactic cluster 1E0657-558. (right) X-ray image of the 78 cluster with redder meaning hotter and higher baryon density. (both) Green 79 contours are reconstruction of gravity contours from weak lensing. White 80 rings are the best fit mass maxima at 68.3%, 95.5%, and 99.7% confidence. 81 The matter maxima of the clusters are clearly separated from x-ray maxima. [9] | 8 |
| 82 | Figure 2.4 | Plank CMB sky. Sky map features small variations in temperature in primor- 83 dial light. These anisotropies are used to make inferences about the universe's 84 energy budget and developmental history. [10] | 9 |
| 85 | Figure 2.5 | Observed Cosmic Microwave Background power spectrum as a function of 86 multipole moment from Plank [10]. Blue line is best fit model from Λ CDM. 87 Red points and lines are data and error, respectively. | 10 |
| 88 | Figure 2.6 | Predicted power spectra of CMB for different $\Omega_m h^2$ values for fixed baryon 89 density from [11]. (left) Low $\Omega_m h^2$ increases the prominence of first and 90 second peaks. (middle) $\Omega_m h^2$ is most similar to the observed power spectrum. 91 The second and third peaks are similar in height. (right) $\Omega_m h^2$ is large which 92 suppresses the first peak and raises the prominence of the third peak. | 10 |
| 93 | Figure 2.7 | The Standard Model (SM) of particle physics. Figure taken from http://www.quantumdiaries.org/2014/03/14/the-standard-model-a-beautiful-but-flawed-theory/ | 12 |
| 96 | Figure 2.8 | Simplified Feynman diagram demonstrating with different ways DM can 97 interact with SM particles. The 'X's refer to the DM particles whereas the 98 SM refer to fundamental particles in the SM. The large circle in the center 99 indicates the vertex of interaction and is purposely left vague. The colored 100 arrows refer to different directions of time as well as their respective labels. 101 The arrows indicate the initial and final state of the DM -SM interaction in time. | 13 |

| | | |
|-----|--|----|
| 102 | Figure 2.9 A single jet event in ATLAS detector from 2017 [16]. Jet momentum was 103 observed to be 1.9 TeV. Missing transverse momentum was observed to be 104 1.9 TeV compared to the initial transverse momentum of the event was 0. 105 Implied MET is traced by a red dashed line in event display. | 14 |
| 106 | Figure 2.10 More detailed pseudo-Feynman diagram of particle cascade from dark matter 107 annihilation into 2 quarks. The quarks hadronize and decay to stable particles 108 like γ or the anti-proton (p^-). Diagram pulled from ICRC 2021 presentation 109 on DM annihilation search [17]. | 15 |
| 110 | Figure 2.11 Dark Matter (DM) decay spectrum for $b\bar{b}$ initial state and γ final state. Redder 111 spectra are for larger DM masses. Bluer spectra are light DM masses. x is a 112 unitless factor defined as the ratio of the mass of DM, m_χ , and the final state 113 particle energy E_γ . Figure from [19]. | 17 |
| 114 | Figure 2.12 Different dark matter density profiles compared. Some models produce ex- 115 ceptionally large densities at small r [20]. | 18 |
| 116 | Figure 2.13 The Milky Way Galaxy in photons (γ) and neutrinos (ν) [22]. The Galactic 117 center is at $l=0^\circ$ and is the brightest region in all panels. (top) An Optical 118 color image of the Milky Way galaxy seen from Earth. Clouds of gas and dust 119 obscure some light from stars. (2nd down) Integrated flux of γ -rays observed 120 by the Fermi-LAT telescope [23]. (middle) Expected neutrino emission 121 that corresponds with Fermi-LAT observations. (2nd up) Expected neutrino 122 emission profile after considering detector systematics of IceCube. (bottom) 123 Observed neutrino emission from region of the galactic plane. Substantial 124 neutrino emission was detected. | 19 |
| 125 | Figure 2.14 Dark Matter annihilation spectra for different final state particle and standard 126 model annihilation channels [24]. Photons (red), e^\pm (green), \bar{p} (blue), ν (black). | 20 |
| 127 | Figure 3.1 TODO: Show a nuclear reactor with cherenkov radiation[NEEDS A SOURCE][FACT 128 CHECK THIS] | 22 |
| 129 | Figure 3.2 TODO: absorption spectrum of liquid and solid water[NEEDS A SOURCE][FACT 130 CHECK THIS] | 23 |

| | | |
|-----|---|----|
| 131 | Figure 7.1 Illustration of the combination technique showing a comparison between 132 $-2 \ln \lambda$ provided by four instruments (colored lines) from the observation 133 of the same dSph without any J nuisance and their sum, <i>i.e.</i> the resulting 134 combined likelihood (thin black line). According to the test statistics of 135 Equation (7.6), the intersection of the likelihood profiles with the line $-2 \ln \lambda$ 136 = 2.71 indicates the 95% C.L. upper limit on $\langle \sigma v \rangle$. The combined likeli- 137 hood (thin black line) shows a smaller value of upper limit on $\langle \sigma v \rangle$ than 138 those derived by individual instruments. We also show the uncertainties on 139 the J -factor affects the combined likelihood and degrade the upper limit on 140 $\langle \sigma v \rangle$ (thick black line). All likelihood profiles are normalized so that the 141 global minimum $\langle \sigma v \rangle$ is 0. We note that each profile depends on the observa- 142 tional conditions in which a target object was observed. The sensitivity of a 143 given instrument can be degraded and the upper limits less constraining if the 144 observations are performed in non optimal conditions such as a high zenith 145 angle or a short exposure time. | 34 |
| 146 | Figure 7.2 HAWC upper limits at 95% confidence level on $\langle \sigma v \rangle$ versus DM mass for 147 seven annihilation channels, using the set of J -factors from Ref. [29] The 148 solid line represents the observed combined limit. Dashed lines represent 149 limits from individual dSphs. | 36 |
| 150 | Figure 7.3 HAWC Brazil bands at 95% confidence level on $\langle \sigma v \rangle$ versus DM mass for 151 seven annihilation channels with J -factors from \mathcal{GS} [29]. The solid line 152 represents the combined limit from 13 dSphs. The dashed line is the expected 153 limit. The green band is the 68% containment. The yellow band is the 95% 154 containment. | 37 |
| 155 | Figure 7.4 Upper limits at 95% confidence level on $\langle \sigma v \rangle$ in function of the DM mass for 156 eight annihilation channels, using the set of J factors from Ref. [29] (\mathcal{GS} set 157 in Table 7.1). The black solid line represents the observed combined limit, 158 the black dashed line is the median of the null hypothesis corresponding 159 to the expected limit, while the green and yellow bands show the 68% and 160 95% containment bands. Combined upper limits for each individual detector 161 are also indicated as solid, colored lines. The value of the thermal relic 162 cross-section in function of the DM mass is given as the red dotted-dashed 163 line [36]. | 39 |
| 164 | Figure 7.5 Same as Fig. 7.4, using the set of J factors from Ref. [31, 35] (\mathcal{B} set in Table 7.1). 40 | |
| 165 | Figure 7.6 Comparisons of the combined limits at 95% confidence level for each of the 166 eight annihilation channels when using the J factors from Ref. [29] (\mathcal{GS} set in 167 Table 7.1), plain lines, and the J factor from Ref. [31, 35] (\mathcal{B} set in Table 7.1), 168 dashed lines. The cross-section given by the thermal relic is also indicated [36]. 41 | |

LIST OF ABBREVIATIONS

- 170 **MSU** Michigan State University
171 **LANL** Los Alamos National Laboratory
172 **DM** Dark Matter
173 **SM** Standard Model
174 **HAWC** High Altitude Water Cherenkov Observatory

175

CHAPTER 1

INTRODUCTION

176 Is the text not rendering right? Ah ok it knows im basically drafting the doc still

CHAPTER 2

177

DARK MATTER IN THE COSMOS

178 2.1 Introduction

179 The dark matter problem can be summarized in part by the following thought experiment.

180 Let us say you are the teacher for an elementary school classroom. You take them on a field
181 trip to your local science museum and among the exhibits is one for mass and weight. The exhibit
182 has a gigantic scale, and you come up with a fun problem for your class.

183 You ask your class, "What is the total weight of the classroom? Give your best estimation to
184 me in 30 minutes, and then we'll check your guess on the scale. If your guess is within 10% of the
185 right answer, we will stop for ice cream on the way back."

186 The students are ecstatic to hear this, and they get to work. The solution is some variation of
187 the following strategy. The students should give each other their weight or best guess if they do
188 not know. Then, all they must do is add each student's weight and get a grand total for the class.
189 The measurement on the giant scale should show the true weight of the class. When comparing
190 the measured weight to your estimation, multiply the measurement by 1.0 ± 0.1 to get the $\pm 10\%$
191 tolerances for your estimation.

192 Two of your students, Sandra and Mario, return to you with a solution.

193 They say, "We weren't sure of everyone's weight. We used 65 lbs. for the people we didn't
194 know and added everyone who does know. There are 30 of us, and we got 2,000 lbs.! That's a ton!"

195 You estimated 1,900 lbs. assuming the average weight of a student in your class was 60 lbs.
196 So, you are pleased with Sandra's and Mario's answer. You instruct your students to all gather on
197 the giant scale and read off the weight together. To all your surprise, the scale reads *10,000 lbs.*!
198 10,000 is significantly more than a 10% error from 2,000. In fact, it is approximately 5 times more
199 massive than either your or your students' estimates. You think to yourself and conclude there
200 must be something wrong with the scale. You ask an employee to check the scale and verify it is
201 well calibrated. They confirm that the scale is in working order. You weigh a couple of students
202 individually to assess that the scale is well calibrated. Sandra weighs 59 lbs., and Mario weighs

203 62 lbs., typical weights for their age. You then weigh each student individually and see that their
204 weights individually do not deviate greatly from 60 lbs. So, where does all the extra weight come
205 from?

206 This thought experiment serves as an analogy to the Dark Matter problem. The important
207 substitution to make however is to replace the students with stars and the classroom with a galaxy,
208 say the Milky Way. Individually the mass of stars is well measured and defined with the Sun as our
209 nearest test case. However, when we set out to measure the mass of a collection of stars as large as
210 galaxies, our well-motivated estimation is wildly incorrect. There simply is no way to account for
211 this discrepancy except without some unseen, or dark, contribution to mass and matter in galaxies.
212 I set out in my thesis to narrow the possibilities of what this Dark Matter could be.

213 This chapter is organized like the following... **TODO: Text should look like ... Chapter x has**
214 **blah blah blah.**

215 **2.2 Dark Matter Basics**

216 Presently, a more compelling theory of cosmology that includes Dark Matter (DM) in order
217 to explain a variety of observations is Λ Cold Dark Matter, or Λ CDM. I present the evidence
218 supporting Λ CDM in Section 2.3 yet discuss the conclusions of the Λ CDM model here. According
219 to Λ CDM fit to observations on the Cosmic Microwave Background (CMB), DM is 26.8% of the
220 universe's current energy budget. Baryonic matter, stuff like atoms, gas, and stars, contributes to
221 4.9% of the universe's current energy budget [1, 2, 3].

222 DM is dark; it does not interact readily with light at any wavelength. DM also does not interact
223 noticeably with the other standard model forces (Strong and Weak) at a rate that is readily observed
224 [3]. DM is cold, which is to say that the average velocity of DM is below relativistic speeds [1].
225 'Hot' DM would not likely manifest the dense structures we observe like galaxies, and instead
226 would produce much more diffuse galaxies than what is observed [3, 1]. DM is old; it played a
227 critical role in the formation of the universe and the structures within it [1, 2].

228 Observations of DM have so far been only gravitational. The parameter space available to what
229 DM could be therefore is extremely broad. The broad DM parameter space is iteratively tested in

230 DM searches by supposing a hypothesis that has not yet been ruled out and performing observations
231 to test them. When the observations yield a null result, the parameter space is constrained further.
232 I present some approaches for DM searches in Section 2.4.

233 **2.3 Evidence for Dark Matter**

234 Dark Matter (DM) has been a looming problem in physics for almost 100 years. Anomalies
235 have been observed by astrophysicists in galactic dynamics as early as 1933 when Fritz Zwicky
236 noticed unusually large velocity dispersion in the Coma cluster. Zwicky's measurement was the
237 first recorded to use the Virial theorem to measure the mass fraction of visible and invisible matter
238 in celestial bodies [4]. From Zwicky in [5], "*If this would be confirmed, we would get the surprising*
239 *result that dark matter is present in much greater amount than luminous matter.*" Zwicky's and
240 others' observation did not instigate a crisis in astrophysics because the measurements did not
241 entirely conflict with their understanding of galaxies [4]. In 1978, Rubin, Ford, and Norbert
242 measured rotation curves for ten spiral galaxies [6]. Rubin et al.'s 1978 publication presented a
243 major challenge to the conventional understanding of galaxies that could no longer be dismissed by
244 measurement uncertainties. Evidence has been mounting ever since for this exotic form of matter.
245 The following subsections provide three compelling pieces of evidence in support of the existence
246 of DM.

247 **2.3.1 First Clues: Stellar Velocities**

248 Zwicky, and later Rubin, measured the stellar velocities of various galaxies to estimate their
249 virial mass. The Virial Theorem upon which these observations are interpreted is written as

$$2T + V = 0. \quad (2.1)$$

250 Where T is the kinetic energy and V is the potential energy in a self-gravitating system. The
251 classical Newton's law of gravity from stars and gas was used for gravitational potential modeled in
252 the observed galaxies:

$$V = -\frac{1}{2} \sum_i \sum_{j \neq i} \frac{m_i m_j}{r_{ij}}. \quad (2.2)$$

253 Zwicky et al. measured just the velocities of stars apparent in optical wavelengths [5]. Rubin et al.
 254 added by measuring the velocity of the hydrogen gas via the 21 cm emission line of Hydrogen [6].
 255 The velocities of the stars and gas are used to infer the total mass of galaxies and galaxy clusters
 256 via Equation (2.1). An inferred mass is obtained from the luminosity of the selected sources. The
 257 two inferences are compared to each other as a luminosity to mass ratio which typically yielded [1]

$$\frac{M}{L} \sim 400 \frac{M_{\odot}}{L_{\odot}} \quad (2.3)$$

258 M_{\odot} and L_{\odot} referring to stellar mass and stellar luminosity, respectively. These ratios clearly indicate
 259 a discrepancy in apparent light and mass from stars and gas and their velocities.

260 Rubin et al. [6] demonstrated that the discrepancy was unlikely to be an underestimation of
 261 the mass of the stars and gas. The inferred "dark" mass was up to 5 times more than the luminous
 262 mass. This dark mass also needed to extend well beyond the extent of the luminous matter.

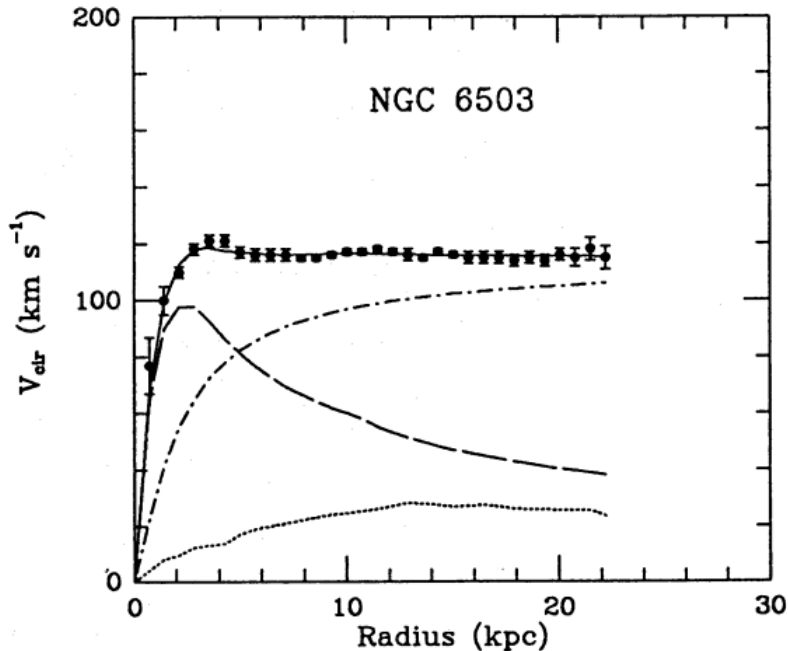


Figure 2.1 Rotation curve fit to NGC 6503 from [7]. Dashed line is the contribution from visible matter. Dotted curves are from gas. Dash-dot curves are from dark matter (DM). Solid line is the composite contribution from all matter and DM sources. Data are indicated with bold dots with error bars. Data agree strongly with a matter + DM composite prediction.

263 Figure 2.1 features one of many rotation curves plotted from the stellar velocities within galaxies.

264 The measured rotation curves mostly feature a flattening of velocities at higher radius which is not
265 expected if the gravity was only coming from gas and luminous matter. The extension of the
266 flat velocity region also indicates that the DM is distributed far from the center of the galaxy.
267 Modern velocity measurements include significantly larger objects, galactic clusters, and smaller
268 objects, dwarf galaxies. Yet, measurements along this regime are leveraging the Virial theorem
269 with Newtonian potential energies. We know Newtonian gravity is not a comprehensive description
270 of gravity. New observational techniques have been developed since 1978, and those are discussed
271 in the following sections.

272 **2.3.2 Evidence for Dark Matter: Gravitational Lensing**

273 Modern evidence for dark matter comes from new avenues beyond stellar velocities. Grav-
274 itational lensing from DM is a new channel from general relativity. General relativity predicts
275 aberrations in light caused by massive objects. In recent decades we have been able to measure the
276 lensing effects from compact objects and DM halos. Figure 2.2 shows how different massive ob-
277 jects change the final image of a faraway galaxy resulting from gravitational lensing. Gravitational
278 lensing developed our understanding of dark matter in two important ways.

279 Gravitational lensing provides additional compelling evidence for DM. The observation of two
280 merging galactic clusters in 2006, shown in Figure 2.3, provided a compelling argument for DM
281 outside the Standard Model. These clusters merged recently in astrophysical time scales. Galaxies
282 and star cluster have mostly passed by each other as the likelihood of their collision is low. Therefore,
283 these massive objects will mostly track the highest mass, dark and/or baryonic, density. Yet, the
284 intergalactic gas is responsible for the majority of the baryonic mass in the systems [4]. These gas
285 bodies will not phase through and will heat up as they collide together. The hot gas is located via
286 x-ray emission from the cluster. Two observations of the clusters were performed independently of
287 each other.

288 The first was the lensing of light around the galaxies due to their gravitational influences.
289 When celestial bodies are large enough, the gravity they exert bends space and time itself. The
290 warped space-time lenses light and will deflect in an analogous way to how glass lenses will bend

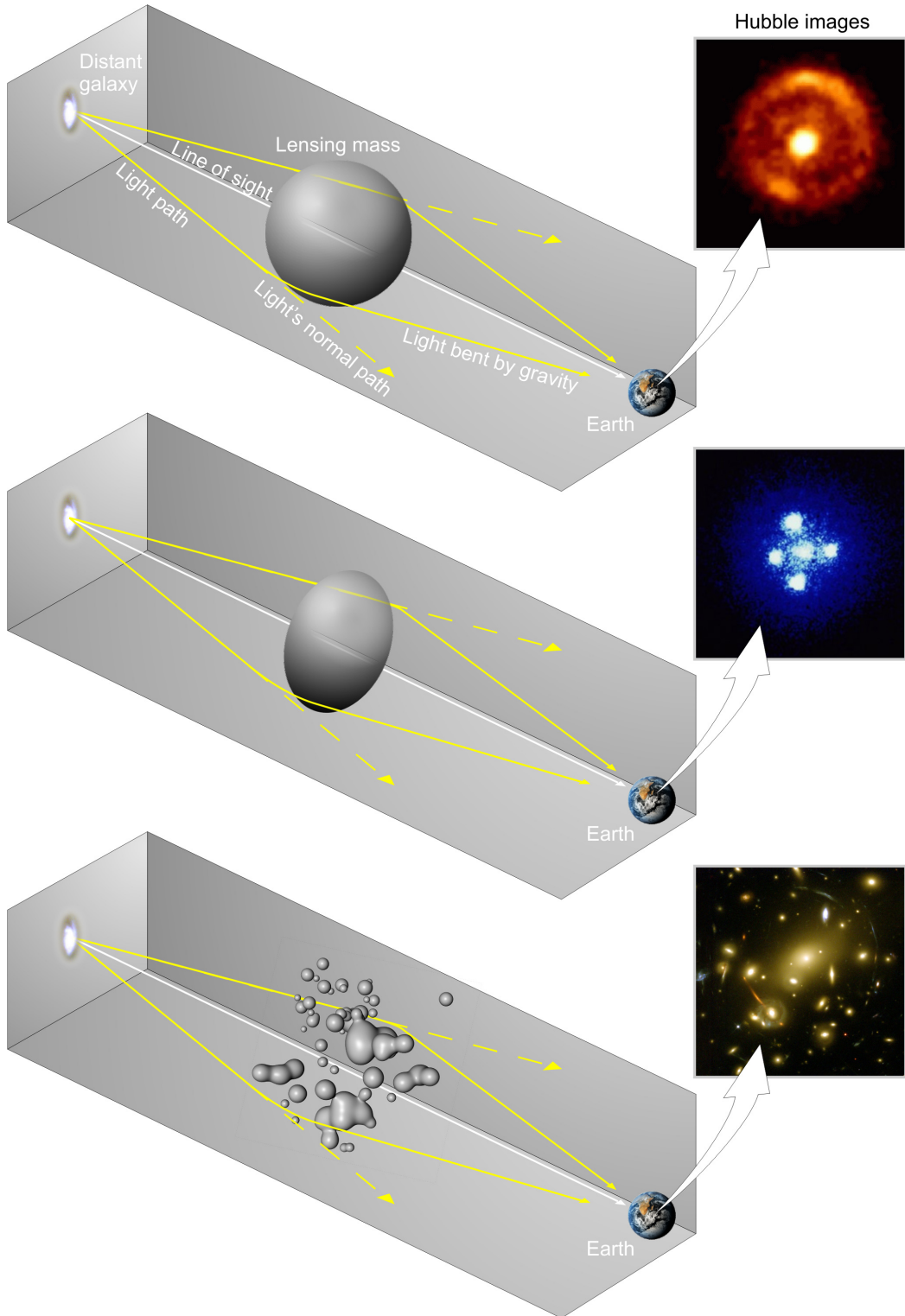


Figure 2.2 Light from distant galaxy is bent in unique ways depending on the distribution of mass between the galaxy and Earth. Yellow dashed lines indicate where the light would have gone if the matter were not present [8].

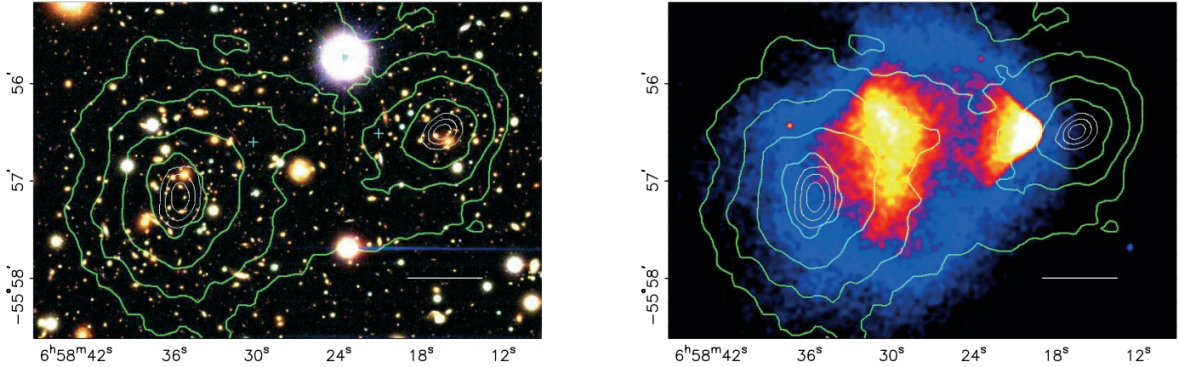


Figure 2.3 (left) Optical image of galactic cluster 1E0657-558. (right) X-ray image of the cluster with redder meaning hotter and higher baryon density. (both) Green contours are reconstruction of gravity contours from weak lensing. White rings are the best fit mass maxima at 68.3%, 95.5%, and 99.7% confidence. The matter maxima of the clusters are clearly separated from x-ray maxima. [9]

291 light, see Figure 2.2. With a sufficient understanding of light sources behind a massive object, we
 292 can reconstruct the contours of the gravitational lenses. The gradient of the contours shown in
 293 Figure 2.3 then indicates how dense the matter is and where it is.

294 The x-ray emission can then be observed from the clusters. Since these galaxies are mostly gas
 295 and are merging, then the gas should be getting hotter. If they are merging, the x-ray emissions
 296 should be the strongest where the gas is mostly moving through each other. Hence, X-ray emission
 297 maps out where the gas is in the merging galaxy cluster.

298 The lensing and x-ray observations were done on the Bullet cluster featured on Figure 2.3.
 299 The x-ray emissions do not align with the gravitational contours from lensing. The incongruence
 300 in mass density and baryon density suggests that there is a lot of matter somewhere that does
 301 not interact with light. Moreover, this dark matter cannot be baryonic [9]. The Bullet Cluster
 302 measurement did not really tell us what DM is exactly, but it did give the clue that DM also does
 303 not interact with itself very strongly. If DM did interact strongly with itself, then it would have been
 304 more aligned with the x-ray emission [9]. There have been follow-up studies of galaxy clusters with
 305 similar results. The Bullet Cluster and others like it provide a persuasive case against something
 306 possibly amiss in our gravitational theories.

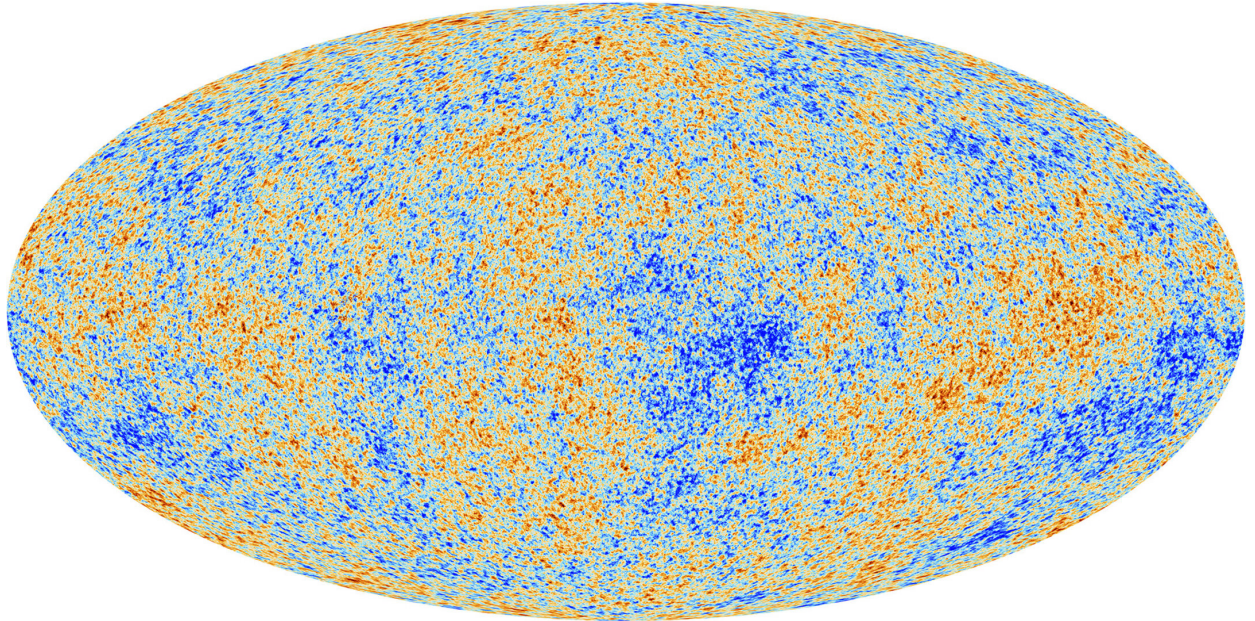


Figure 2.4 Plank CMB sky. Sky map features small variations in temperature in primordial light. These anisotropies are used to make inferences about the universe’s energy budget and developmental history. [10]

307 **2.3.3 Evidence for Dark Matter: Cosmic Microwave Background**

308 The Cosmic Microwave Background (CMB) is the primordial light from the early universe
309 when Hydrogen atoms formed from the free electron and proton soup in the early universe. The
310 CMB is the earliest light we can observe; released when the universe was about 380,000 years old.
311 Then we look at how the simulated universes look like compared to what we see. Figure 2.4 is the
312 most recent CMB image from the Plank satellite after subtracting the average value and masking the
313 galactic plane [10]. Redder regions indicate a slightly hotter region in the CMB, and blue indicates
314 colder. The intensity variations are on the order of 1 in 1000 with respect to the average value.

315 The Cosmic Microwave Background shows that the universe had DM in it from an incredibly
316 early stage. To measure the DM, Dark Energy, and matter fractions of the universe from the CMB,
317 the image is analyzed into a power spectrum, which shows the amplitude of the fluctuations as
318 a function of spherical multipole moments. Λ CDM provides the best fit to the power spectra of
319 the CMB as shown in Figure 2.5. The CMB power spectrum is quite sensitive to the fraction
320 of each energy contribution in the early universe. Low l modes are dominated by variations
321 in gravitational potential. Intermediate l emerge from oscillations in photon-baryon fluid from

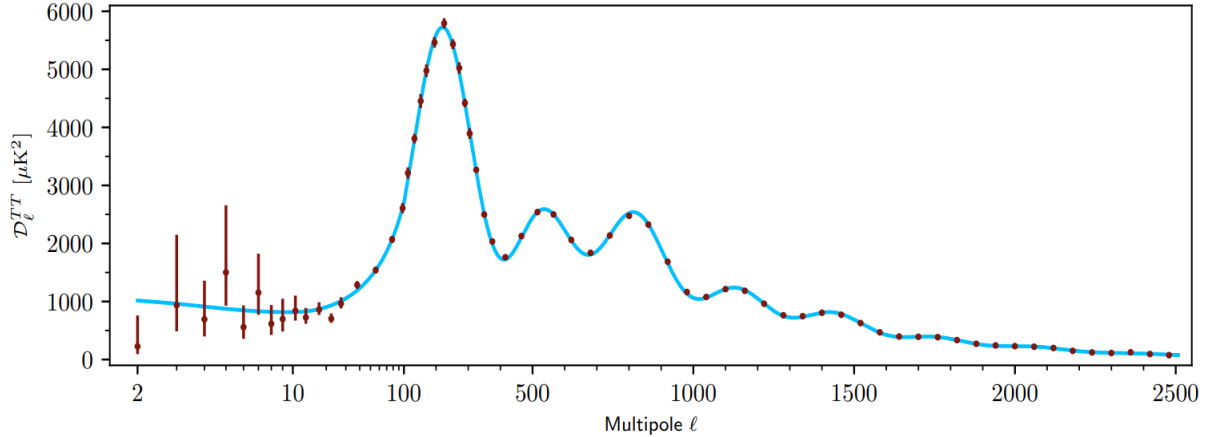


Figure 2.5 Observed Cosmic Microwave Background power spectrum as a function of multipole moment from Plank [10]. Blue line is best fit model from Λ CDM. Red points and lines are data and error, respectively.

322 competing baryon pressures and gravity. High l is a damped region from the diffusion of photons
 323 during electron-proton recombination. [1]

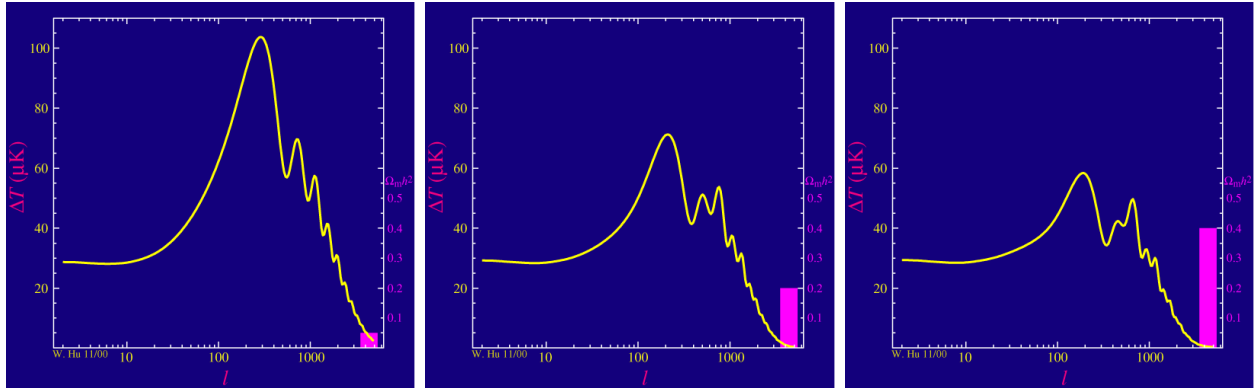


Figure 2.6 Predicted power spectra of CMB for different $\Omega_m h^2$ values for fixed baryon density from [11]. (left) Low $\Omega_m h^2$ increases the prominence of first and second peaks. (middle) $\Omega_m h^2$ is most similar to the observed power spectrum. The second and third peaks are similar in height. (right) $\Omega_m h^2$ is large which suppresses the first peak and raises the prominence of the third peak.

324 The harmonics would look quite different for a universe with less DM. Figure 2.6 demonstrates
 325 the effect $\Omega_m h^2$ has on the expected power spectrum for fixed baryon matter density. [11] Sweeping
 326 $\Omega_m h^2$ in this way clearly shows the effect dark matter has on the CMB power spectrum. The
 327 observations fit well with the Λ CDM model, and the derived fractions are as follows. The matter
 328 fraction: $\Omega_m = 0.3153$; and the baryon fraction: $\Omega_b = 0.04936$ [10]. Plank's observations also
 329 provide a measure of the Hubble constant, H_0 . H_0 especially has seen a growing tension in the

330 past decade that continues to deepened with observations from instruments like the James Webb
331 Telescope [12, 13]. As Hubble tensions deepen, we may find that perhaps Λ **CDM**, despite its
332 successes, is missing some critical physics.

333 Overall, the Newtonian motion of stars in galaxies, weak lensing from galactic clusters, and
334 power spectra from primordial light form a compelling body of research in favor of dark matter.
335 It takes another leap of theory and experimentation to make observations of DM that are non-
336 gravitational in nature. In Section 2.3, the evidence for DM implies strongly that the DM is matter
337 and not a lost parameter in the gravitational fields between massive objects. Finally, if we take one
338 axiom: that this matter has quantum behavior, such as being described by some Bohr wavelength
339 and abiding by some fermion or boson statistics; then we arrive at particle dark matter. One particle
340 DM hypothesis is the Weakly Interacting Massive Particle (WIMP). This DM candidate theory is
341 discussed further in the next section and is the focus of this thesis.

342 **2.4 Searching for Dark Matter: Particle DM**

343 Section 2.4 shows the Standard Model of particle physics and is currently the most accurate
344 model for the dynamics of fundamental particles like electrons and photons. The current status
345 of the SM does not have a viable DM candidate. When looking at the standard model, we can
346 immediately exclude any charged particle because charged particles interact strongly with light.
347 Specifically, this will rule out the following charged, fundamental particles: $e, \mu, \tau, W, u, d, s, c, t, b$
348 and their corresponding antiparticles. Recalling from Section 2.2 that DM must be long-lived and
349 stable over the age of the universe which excludes all SM particles with decay half-lives at or shorter
350 than the age of the universe. The lifetime constraint additionally eliminates the Z and H bosons.
351 Finally, the candidate DM needs to be somewhat massive. Recall from Section 2.2 that DM is cold
352 or not relativistic through the universe. This eliminates the remaining SM particles: $\nu_{e,\mu,\tau}, g, \gamma$ as
353 DM candidates. Because there are no DM candidates within the SM, the DM problem strongly
354 hints to physics beyond the SM (BSM).

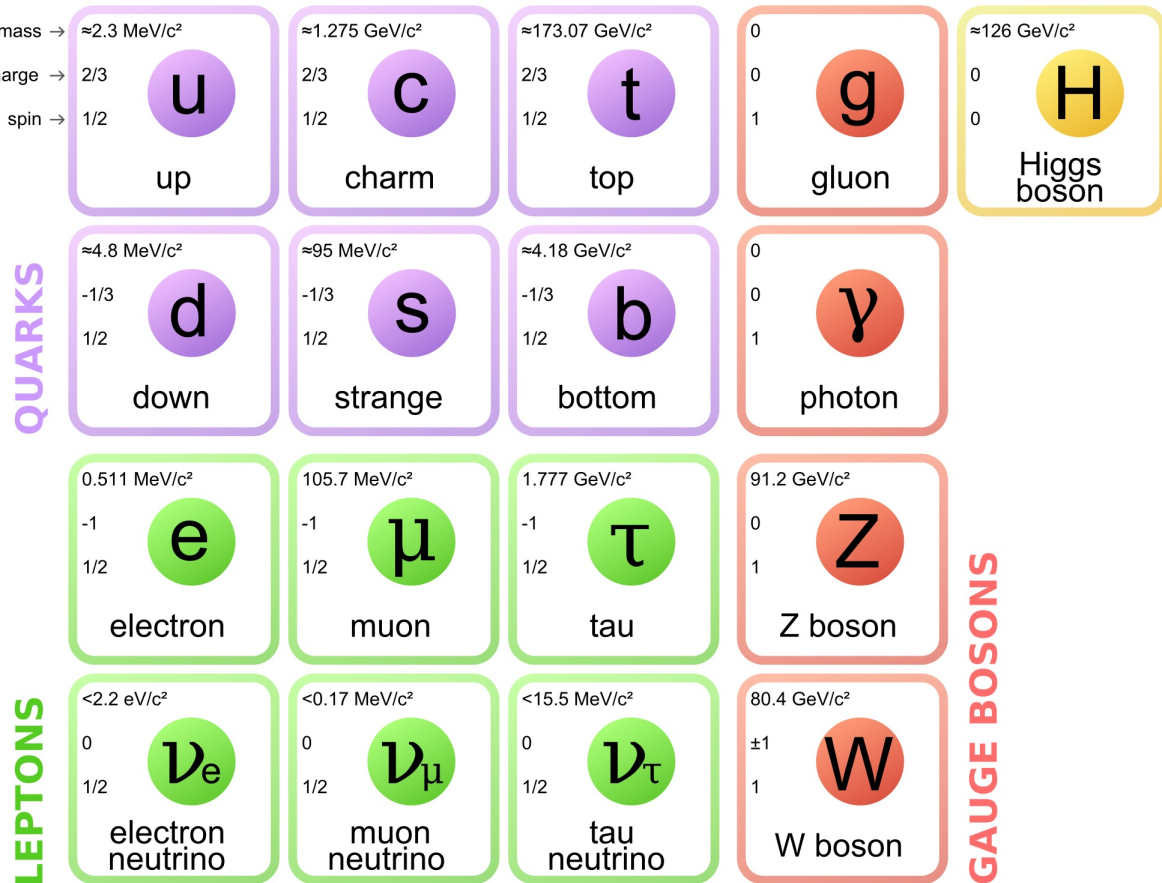


Figure 2.7 The Standard Model (SM) of particle physics. Figure taken from <http://www.quantumdiaries.org/2014/03/14/the-standard-model-a-beautiful-but-flawed-theory/>

355 2.4.1 Shake it, Break it, Make it

356 When considering DM that couples in some way with the SM, the interactions are roughly
 357 demonstrated by interaction demonstrated in Figure 2.8. The figure is a simplified Feynman
 358 diagram where the arrow of time represents the interaction modes of: **Shake it, Break it, Make it**.

359 **Shake it** refers to the direct detection of dark matter. Direct detection interactions start with
 360 a free DM particle and an SM particle. The DM and SM interact via elastic or inelastic collision
 361 and recoil away from each other. The DM remains in the dark sector and imparts some momentum
 362 onto the SM particle. The hope is that the momentum imparted onto the SM particle is sufficiently
 363 high enough to pick up with extremely sensitive instruments. Because we cannot create the DM in
 364 the lab, a direct detection experiment must wait until DM is incident on the detector. Most direct
 365 detection experiments are therefore placed in low-background environments with inert detection

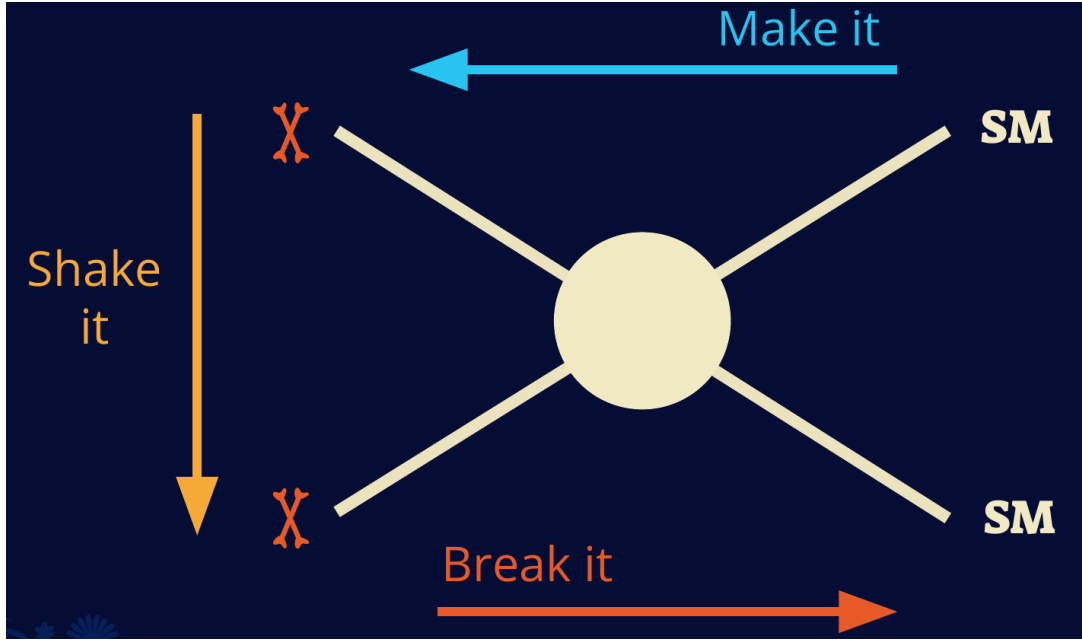


Figure 2.8 Simplified Feynman diagram demonstrating different ways DM can interact with SM particles. The 'X's refer to the DM particles whereas the SM refer to fundamental particles in the SM. The large circle in the center indicates the vertex of interaction and is purposely left vague. The colored arrows refer to different directions of time as well as their respective labels. The arrows indicate the initial and final state of the DM -SM interaction in time.

³⁶⁶ media like the noble gas Xenon. [14]

³⁶⁷ **Make it** refers to the production of DM from SM initial states. The experiment starts with
³⁶⁸ particles in the SM. These SM particles are accelerated to incredibly high energies and then collide
³⁶⁹ with each other. In the confluence of energy, DM hopefully emerges as a byproduct of the SM
³⁷⁰ annihilation. Often it is the collider experiments that are energetic enough to hypothetically produce
³⁷¹ DM. These experiments include the world-wide collaborations ATLAS and CMS at CERN where
³⁷² proton collide together at extreme energies. The DM searches, however, are complex. DM likely
³⁷³ does not interact with the detectors and lives long enough to escape the detection apparatus of
³⁷⁴ CERN's colliders. This means any DM production experiment searches for an excess of events
³⁷⁵ with missing momentum or energy in the events. An example event with missing transverse
³⁷⁶ momentum is shown in Figure 2.9. The missing momentum with no particle tracks implies a
³⁷⁷ neutral particle carried the energy out of the detector. However, there are other neutral particles
³⁷⁸ in the SM, like neutrons or neutrinos, so any analysis has to account for SM signatures of missing

379 momentum. [15]

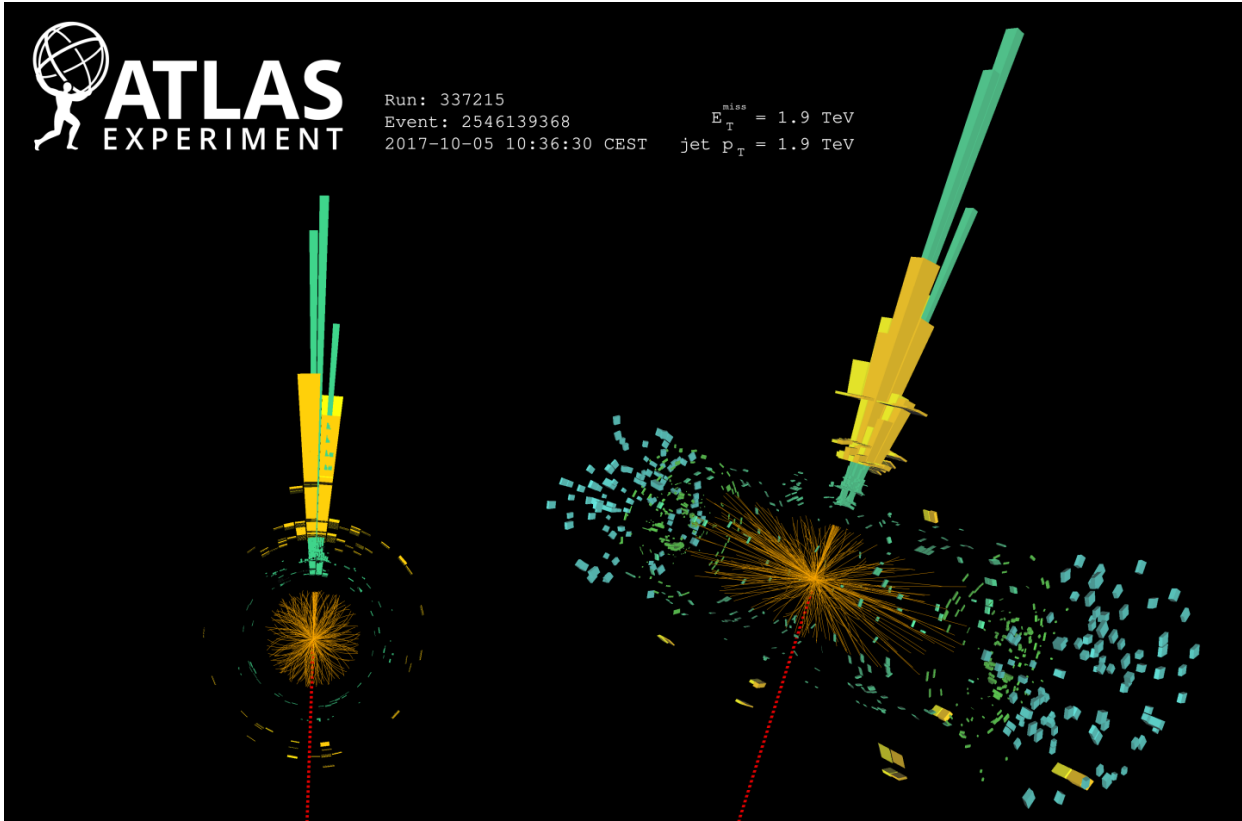


Figure 2.9 A single jet event in ATLAS detector from 2017 [16]. Jet momentum was observed to be 1.9 TeV. Missing transverse momentum was observed to be 1.9 TeV compared to the initial transverse momentum of the event was 0. Implied MET is traced by a red dashed line in event display.

380 **2.4.2 Break it: Standard Model Signatures of Dark Matter through Indirect Searches**

381 **Break it** refers to the creation of SM particles from the dark sector, and it is the primary focus
382 of this thesis. The interaction begins with DM or in the dark sector. The hypothesis is that this
383 DM will either annihilate with itself or decay and produce an SM byproduct. This method is
384 often referred to as the Indirect Detection of DM because we have no lab to directly control or
385 manipulate the DM. Therefore, most indirect DM searches are performed using observations of
386 known DM densities among the astrophysical sources. The strength is that we have the whole of the
387 universe and its 13.6-billion-year lifespan to use as a detector and particle accelerator. Additionally,
388 locations of dark matter are well cataloged since it was astrophysical observations that presented

389 the problem of DM in the first place.

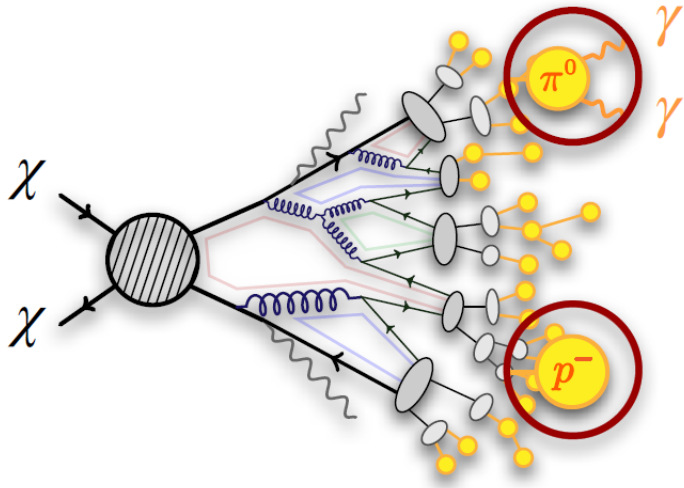


Figure 2.10 More detailed pseudo-Feynman diagram of particle cascade from dark matter annihilation into 2 quarks. The quarks hadronize and down to stable particles like γ or the anti-proton (p^-). Diagram pulled from ICRC 2021 presentation on DM annihilation search [17].

390 However, anything can happen in the universe. There are many difficult to deconvolve back-
391 grounds when searching for DM. One prominent example is the galactic center. We know the
392 galactic center has a large DM content because of stellar kinematics in our Milky Way and DM halo
393 simulations. Yet, any signal from the galactic center is challenging to parse apart from the extreme
394 environment of our supermassive black hole, unresolved sources, and diffuse emission from the
395 interstellar medium [18]. Despite the challenges, any DM model that yields evidence in the other
396 two observation methods, **Shake it or Make it** must be corroborated with indirect observations of
397 the known DM sources. Without corroborating evidence, DM observation in the lab is hard-pressed
398 to demonstrate that it is the model contributing to the DM seen at the universal scale.

399 In the case of WIMP DM, signals are described in terms of primary SM particles produced
400 from DM decay or annihilation. The SM initial state particles are then simulated down to stable
401 final states such as the γ , ν , p , or e which can traverse galactic lengths to reach Earth.

402 Figure 2.10 shows the quagmire of SM particles that emerges from SM initial states that are not
403 stable [17]. There are many SM particles with varying energies that can be produced in such an

404 interaction. For any arbitrary DM source and stable SM particle, the SM flux from DM annihilating
 405 to a neutral particle in the SM, ϕ , from a region in the sky is described by the following.

$$\frac{d\Phi_\phi}{dE_\phi} = \frac{\langle\sigma v\rangle}{8\pi m_\chi^2} \frac{dN_\phi}{dE_\phi} \times \int_{\text{source}} d\Omega \int_{l.o.s} \rho_\chi^2 dl(r, \theta') \quad (2.4)$$

406 In Equation (7.1), $\langle\sigma v\rangle$ is the velocity-weighted annihilation cross-section of DM to the SM. m_χ
 407 refers to the mass of DM, noted with Greek letter χ . $\frac{dN_\phi}{dE_\phi}$ is the N particle flux weighted by the
 408 particle energy. An example is provided in Figure 2.11 for the γ final state. The integrated terms
 409 are performed over the solid angle, $d\Omega$, and line of sight, l.o.s. ρ is the density of DM for a
 410 location (r, θ') in the sky. The terms left of the '×' are often referred to as the particle physics
 411 component. The terms on the right are referred to as the astrophysical component. For decaying
 412 DM, the equation changes to...

$$\frac{d\Phi_\phi}{dE_\phi} = \frac{1}{4\pi\tau m_\chi} \frac{dN_\phi}{dE_\phi} \times \int_{\text{source}} d\Omega \int_{l.o.s} \rho_\chi dl(r, \theta') \quad (2.5)$$

413 In Equation (2.5), τ is the decay lifetime of the DM. Just as in Equation (7.1), the left and
 414 right terms are the particle physics and the astrophysical components respectively. The integrated
 415 astrophysical component of Equation (7.1) is often called the J-Factor. Whereas the integrated
 416 astrophysical component of Equation (2.5) is often called the D-Factor.

417 Exact DM $\text{DM} \rightarrow \text{SM SM}$ branching ratios are not known, so it is usually assumed to go 100%
 418 into an SM particle/anti-particle. Additionally, when a DM annihilation or decay produces one of
 419 the neutral, long-lived SM particles (ν or γ), the particle is traced back to a DM source. For DM
 420 above GeV energies, there are very few SM processes that can produce particles with such a high
 421 energy. Seeing such a signal would almost certainly be an indication of the presence of dark matter.
 422 Fortunately, the universe provides us with the largest volume and lifetime ever for a particle physics
 423 experiment.

424 2.5 Sources for Indirect Dark Matter Searches

425 The first detection of DM relied on optical observations. Since then, we have developed new
 426 techniques to find DM dense regions. As described in Section 2.3.1, many DM dense regions were
 427 through observing galactic rotation curves. Our Milky Way galaxy is among DM dense regions

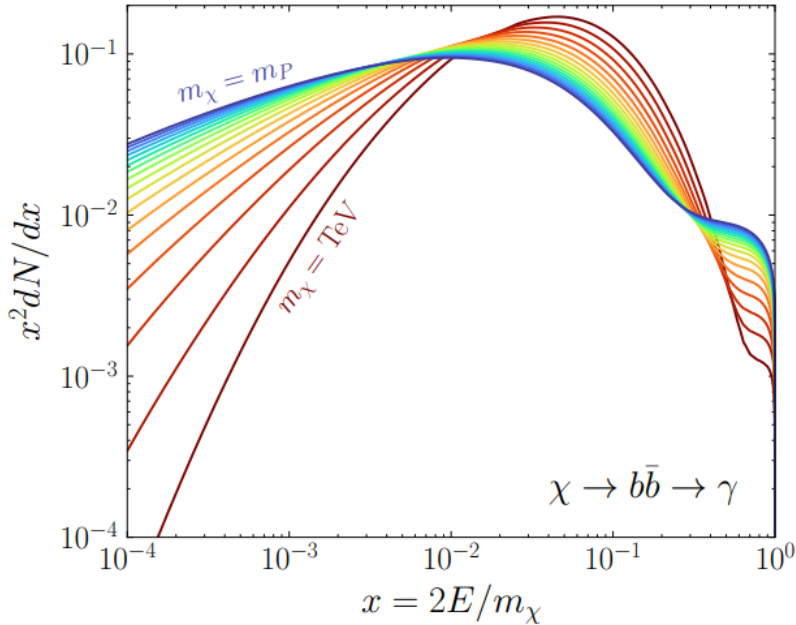


Figure 2.11 Dark Matter (DM) decay spectrum for $b\bar{b}$ initial state and γ final state. Redder spectra are for larger DM masses. Bluer spectra are light DM masses. x is a unitless factor defined as the ratio of the mass of DM, m_χ , and the final state particle energy E_γ . Figure from [19].

discovered, and it is the largest nearby DM dense region to look at. Additionally, the DM halo surrounding the Milky Way is clumpy [18]. There are regions in the DM halo of the Milky Way that have more DM than others that have captured gas over time. These sub-halos were dense enough collapse gas and form stars. These apparent sub galaxies are known as dwarf spheroidal galaxies and are the main sources studied in this thesis. Each source type comes with different trade-offs. Galactic Center studies will be very sensitive to the assumed distribution of DM. The central DM density can vary substantially as demonstrated in Figure 2.12. At distances close to the center of the galaxy, or small r , the differences in DM densities can be 3-4 orders of magnitude. Searches toward the galactic center will therefore be quite sensitive to the assumed DM distribution.

Searches toward Dwarf Spheroidal Galaxies (dSph's) suffer from uncertainties in the DM density less than the galactic center studies. This is mostly from their diminutive size being smaller than the angular resolution of most γ -ray observatories [18]. The DM content dSph's are typically determined with the Virial theorem, Equation (2.1), and are usually majority DM [18] in mass. DSph's tend to be ideal sources to look at for DM searches. Their environments are quiet with little

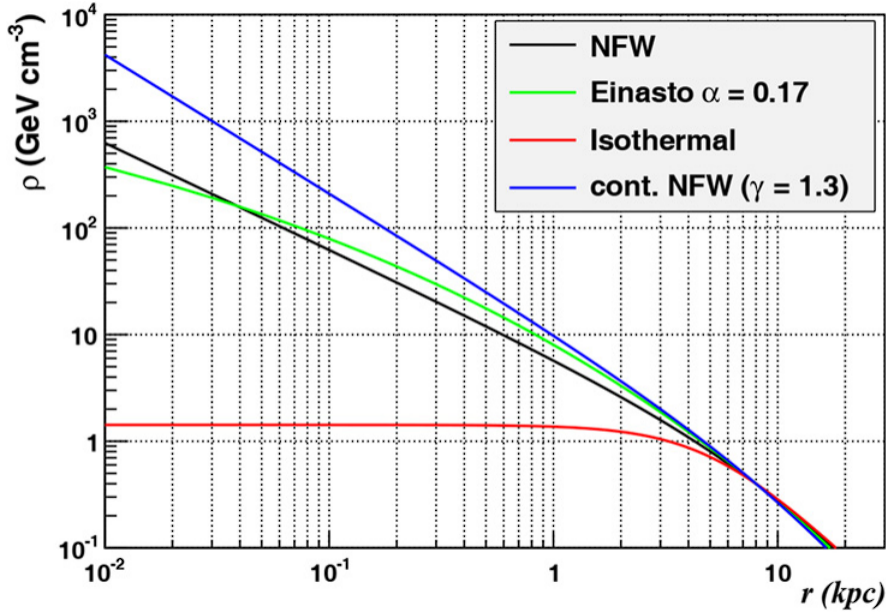


Figure 2.12 Different dark matter density profiles compared. Some models produce exceptionally large densities at small r [20].

442 astrophysical background. Unlike the galactic center, the most active components of dSph's are the
 443 stars within them versus a violent accretion disc around a black hole. All this together means that
 444 dSph's are among the best sources to look at for indirect DM searches. dSph's are the targets of
 445 focus for this thesis.

446 2.6 Multi-Messenger Dark Matter

447 Astrophysics entered a new phase in the past few decades that leverages our increasing sensitivity
 448 to SM channels and general relativity (GR). Up until the 21st century, astrophysical observations
 449 were performed with photons (γ) only. Astrophysics with this 'messenger' is fairly mature now.
 450 Novel observations of the universe have since only adjusted the sensitivity of the wavelength of
 451 light that is observed except at MeV energies. Gems like the CMB [10], and more have ultimately
 452 been observations of different wavelengths of light. Multi-messenger astrophysics proposes using
 453 other SM particles such the p^{+-} , or ν or gravitation waves predicted by general relativity.

454 The experiment LIGO had a revolutionary discovery in 2016 with the first detection of a binary
 455 black hole merger [21]. This opened the collective imagination to observing the universe through
 456 gravitational waves. There has also been a surge of interest in the neutrino (ν) sector. IceCube

457 demonstrated that we are sensitive to neutrinos in regions that correlate with significant photon
 458 emission like the galactic plane [22]. Neutrinos, like gravitational waves and light, travel mostly
 459 unimpeded from their source to our observatories. This makes pointing to the originating source
 460 of these messengers much easier than it is for cosmic rays which are deflected from their source by
 461 magnetic fields.

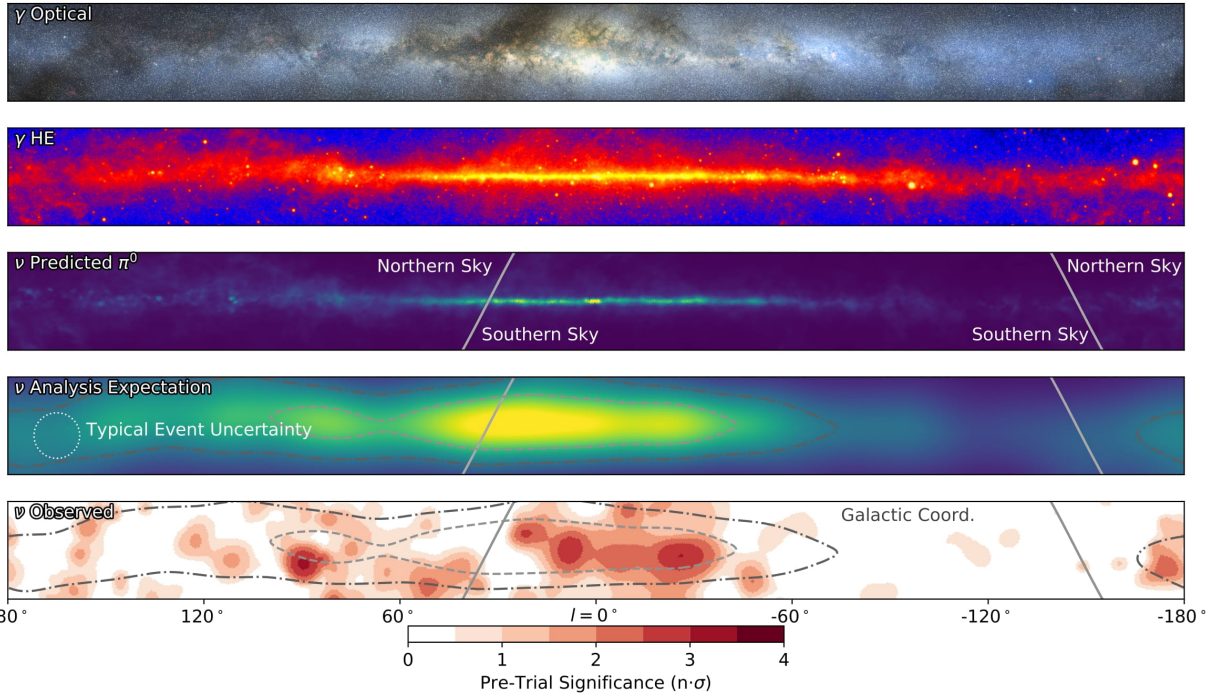


Figure 2.13 The Milky Way Galaxy in photons (γ) and neutrinos (ν) [22]. The Galactic center is at $l=0^\circ$ and is the brightest region in all panels. (top) An Optical color image of the Milky Way galaxy seen from Earth. Clouds of gas and dust obscure some light from stars. (2nd down) Integrated flux of γ -rays observed by the Fermi-LAT telescope [23]. (middle) Expected neutrino emission that corresponds with Fermi-LAT observations. (2nd up) Expected neutrino emission profile after considering detector systematics of IceCube. (bottom) Observed neutrino emission from region of the galactic plane. Substantial neutrino emission was detected.

462 The IceCube collaboration recently published a groundbreaking result of the Milky Way in
 463 neutrinos. The recent result from IceCube, shown in Figure 2.13, proves that we can make
 464 observations under different messenger regimes. The top two panels show the appearance of the
 465 galactic plane to different wavelengths of light. Some sources are more apparent in some panels,
 466 while others are not. This new channel is powerful because neutrinos are readily able to penetrate
 467 through gas and dust in the Milky Way. This new image also refines our understanding of how high

468 energy particles are produced. For example, the fit to IceCube data prefers neutrino production
 469 from the decay of π^0 [22].

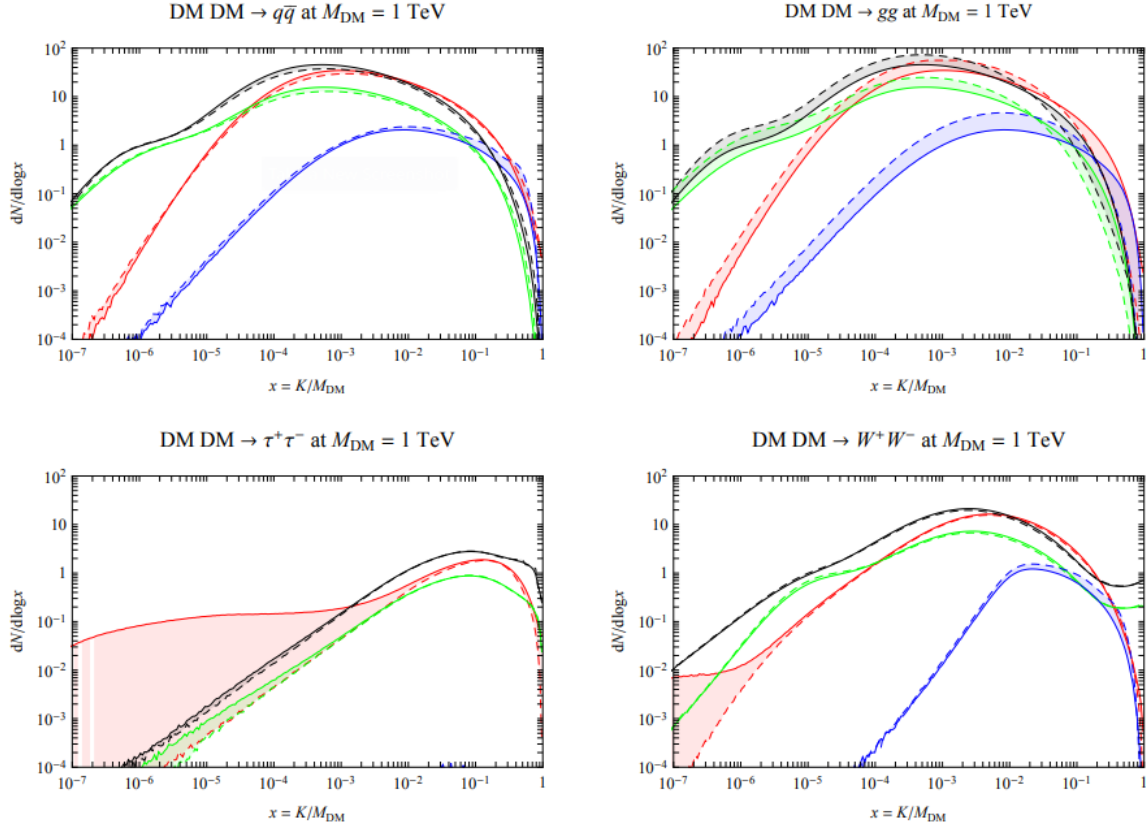


Figure 2.14 Dark Matter annihilation spectra for different final state particle and standard model annihilation channels [24]. Photons (red), e^\pm (green), \bar{p} (blue), ν (black).

470 Exposing our observations to more cosmic messengers greatly increases our sensitivity to
 471 rare processes. In the case of DM, Figure 2.14, there are many SM particles produced in DM
 472 annihilation. Among the final state fluxes are gammas and neutrinos. Charged particles are also
 473 produced however they would not likely make it to Earth since they will be deflected by magnetic
 474 fields between the source and Earth. This means observatories that can see the neutral messengers
 475 are especially good for DM searches and for combining data for a multi-messenger DM search.

CHAPTER 3

476 MULTIMESSENGER ASTROPHYSICS: DETECTING HIGH ENERGY NEUTRAL 477 MESSENGERS

478 3.1 Introduction

479 Before the 20th century, all asttrophysics observations were optical in nature. We litterly only
480 saw things with highly magnified optical observations. Then we discovered cosmic rays. cosmic
481 rays are charged particles, typically naked protons or H+. This was seen by Victor Hess in 19??.
482 Around the same time we discovered neutrinos from beta decay. Sometime around 1950 we started
483 to build neutrino detectors which were mostly sensitive to neutrinos from the sun. Finally, it was
484 theorized that compact objects like black holes and neutron stars would create waves in space-time
485 when they experience mergers or collisions.

486 In the 21st century, we have developed new observation techniques and detectors that are no only
487 sensitive to these four messengers - photons (TODO: photon), neutrinos (TODO: nu), Cosmic
488 Rays (CR), and Gravitational Wave (WV) - we're collect high energy versions of these events.
489 For the standad model particles, we're now sensitive to all messengers above the MeV eneryg
490 range. Additionally, the GW's were sensitive to are in the stellar mass black hole region and above
491 within our galactic neighborhood. This means were becoming sensitive to the fundamental physics
492 occuring within the universe and we can rely on the universe as a TeV+ particle accelerator. We
493 also have the abaility to correlate high energy events across messengers and gain new insights on
494 the processes that occur in our universe.

495 This thesis focuses on very high energy (VHE) gamma rays and neutrinos. These can both be
496 observed through the water cherenkov detection technique altho not exclusively. Methods on how
497 to detect and observe these neutral messengers are discussed Section 3.3 and Section 3.4

498 3.2 Charged Particles in a Medium

499 For high enery gamma-rays and neutrinos, we can exploit the same effect that charged particles
500 have with water. This effect is known as Cherenkov radiation. Cherenkov Radiation occurs when a
501 charged particle, usually electrons (e) or muons (μ), traverse a medium, like water, faster than the

502 speed of light in that medium. This is similar to sonic boom where an object moves through air
503 faster than the speed of sound in air. Cherenkov radiation can therefore be thought of as an 'optic
504 boom'. Many astro-particle physics experiments will use water as the medium as because water
505 has a unique set of properties ideal for charged particle tracking.



Figure 3.1 TODO: Show a nuclear reactor with cherenkov radiation[NEEDS A SOURCE][FACT CHECK THIS]

506 The frequency of light emitted due to cherenkov radiation follows the equation:

$$INSERT\ Cherenkov\ wavelength\ calc\ HERE. \quad (3.1)$$

507 The absorption spectra is shown in the following figure:

508 **3.3 Photons (γ)**

509 **3.4 Neutrinos (ν)**

510 **3.5 Opportunities to Combine for Dark Matter**



Figure 3.2 TODO: absorption spectrum of liquid and solid water[NEEDS A SOURCE][FACT CHECK THIS]

CHAPTER 4

511 **HIGH ALTITUDE WATER CHERENKOV (HAWC) OBSERVATORY**

512 **4.1 The Detector**

513 **4.2 Events Reconstruction and Data Acquisition**

514 **4.2.1 G/H Discrimination**

515 **4.2.2 Angle**

516 **4.2.3 Energy**

517 **4.3 Remote Monitoring**

518 **4.3.1 ATHENA Database**

519 **4.3.2 HOMER**

520

CHAPTER 5

ICECUBE NEUTRINO OBSERVATORY

521 **5.1 The Detector**

522 **5.2 Events Reconstruction and Data Acquisition**

523 **5.2.1 Angle**

524 **5.2.2 Energy**

525 **5.3 Northern Test Site**

526 **5.3.1 PIgeon remote dark rate testing**

527 **5.3.2 Bulkhead Construction**

CHAPTER 6

COMPUTATIONAL TECHNIQUES IN PARTICLE ASTROPHYSICS

529 **6.1 Neural Networks for Gamma/Hadron Separation**

530 **6.2 Parallel Computing for Dark Matter Analyses**

531

CHAPTER 7

GLORY DUCK

532 **7.1 Dataset and Background**533 **7.1.1 Data Files**

- 534 • Detector Resolution: `response_aerie_svn_27754_systematics_best_mc_test_no`
 535 `broadpulse_10pctlogchargesmearing_0.63qe_25kHzNoise_run5481_curvatu`
 536 `re0_index3.root`
- 537 • Data Map: `maps-20180119/liff/maptree_1024.root`

538 **7.1.2 Data Set Chosen**

539 The maps used for this analysis contain 1017 days of data between runs 2104 (2014-11-26) and
 540 7476 (2017-12-20). They were generated from pass 4.0 reconstruction. The analysis is performed
 541 using the f_{hit} energy binning scheme with bins [1-9] similar to what was done for the Crab and
 542 previous HAWC dSph analysis. [25, 26].

543 **7.1.3 Background Estimation**

544 This analysis was done on dwarf spheroidal (dSph) galaxies because of their large dark matter
 545 (DM) content relative to baryonic. We consider the following to estimate the background to this
 546 study.

- 547 • The dSphs are small in HAWC’s field of view, so the analysis is not sensitive to large or small
 548 scale anisotropies.
- 549 • The dSphs used in this analysis are off the galactic plane.
- 550 • The dSphs are baryonically faint relative to their expected dark matter content and are not
 551 expected to contain gamma-ray sources.

552 Therefor we make no additional assumptions of the background coming from our sources and
 553 use HAWC’s standard direct integration method for background estimation. It is possible for gamma

554 rays from DM annihilation to scatter in transit to HAWC via Inverse Compton Scattering (ICS).
555 This was investigated and its impact on the flux is basically zero. Supporting information on this
556 is in **TODO: refer to appdx**

557 **7.1.4 Software Tools and Development**

558 This analysis was performed using HAL and 3ML, in Python version 2.[25, 27] Dan developed
559 a source model to implement the *Poor Particle Physicists' Cookbook* (PPPC) [28] into HAWC
560 software. This model and corresponding Monte Carlo simulation was consolidated into a dictionary
561 for other collaborators. A NumPy version of this dictionary was made for both Py2 and Py3. The
562 code base for creating this dictionary is also in Dan's sandbox:

- 563 • Py2: <https://gitlab.com/hawc-observatory/sandboxes/salaza82/glory-duc>
564 k-hawc/-/tree/master/GD_spectrumDictionary Generator (Deprecated)
- 565 • Py3: <https://gitlab.com/hawc-observatory/sandboxes/salaza82/pppc2dict>
566 tPPPC2Dict

567 The analysis was performed using the f_{hit} framework performed in the Crab paper[25]. The
568 PPPC model selected for this analysis included electroweak corrections. Dictionaries for the
569 non-electroweak model were generated but not used for this analysis. The Python2 NumPy dictio-
570 nary file for gamma-ray final states is `dmCirSpecDict.npy`. The corresponding Python3 file is
571 `DM_CirrelliSpectrum_dict_gammas.npy`. These files can also be used for decay channels and
572 the PPPC describes how. [28]. Python's pickle is not backwards compatible, so scripts run in Py3
573 are not able to use dictionaries generated using Py2 and vice-versa.

574 All other software used for data analysis, DM profile generation, and job submission to SLURM
575 are also kept in my sandbox for <https://gitlab.com/hawc-observatory/sandboxes/sal>
576 aza82/glory-duck-hawc the Glory Duck project. They're broad descriptions are as follows:

- 577 • `GD_mass_profiles`: scripts that generate .fits maps for HAWC HAL according to [29].
578 Also contains simple plots of these maps.

- 579 • `GD_spectrum`: scripts that generate NumPy dictionaries of PPPC gamma spectra [28].
- 580 • `analysis_scripts`: HAL scripts for performing likelihood computation on HAWC data or
581 simulation with GD spectra and mass profiles.
- 582 • `pointing`: HAL scripts used to compare the impact of point systematic.
- 583 • `poisson_maps`: scripts for generating and managing poisson trials used for this study.

584 **7.2 Analysis**

585 **7.2.1 Monte Carlo Simulation**

586 The expected differential photon flux from a DM-DM annihilation to standard model particles
587 over solid angle is described by the familiar equation.

$$\frac{d\Phi_\gamma}{dE_\gamma} = \frac{\langle\sigma v\rangle}{8\pi m_\chi^2} \frac{dN_\gamma}{dE_\gamma} \times \int_{\text{source}} d\Omega \int_{l.o.s} \rho_\chi^2 dl(r, \theta') \quad (7.1)$$

588 here $\langle\sigma v\rangle$ is the velocity weighted annihilation cross-section. $\frac{dN}{dE}$ is the expected differential number
589 of photons produced at each energy per annihilation. M_χ is the rest mass of the supposed DM
590 particle. J is the astrophysical J-factor and is defined as

591 ρ_χ is the DM density. For this value, we import the PPPC with electroweak corrections [28].
592 The spectrum is implemented as a model script in astromodels for 3ML. The J-factor profiles for
593 each source is imported from Geringer-Sameth (\mathcal{GS}) [30]. Another DM distribution model from
594 Bonnivard (\mathcal{B}) [31] was used for the complete study. However, to save computational time, limits
595 from \mathcal{GS} were scaled to \mathcal{B} instead of each experiment performing a full study a second time. We
596 create NSIDE 16384 maps of the J-factors for each dSph. These maps are integrated over every
597 spatial bin and passed to the fitting software. Plots of these maps are provided for each source in
598 the sandbox directory: `GD_mass_profiles`.

599 **7.2.2 Source Selection and Annihilation Channels**

600 We use many of the dSph presented in our previous dSph DM search [26]. HAWC's sources
601 for Glory Duck include Boötes I, Coma Berenices, Canes Venatici I + II, Draco, Hercules, Leo I,

602 II, + IV, Segue 1, Sextans, and Ursa Major I + II. A full description of all sources used in Glory
 603 Duck is found in Table 7.1. Triangulum II was excluded from the Glory Duck analysis because
 604 of large uncertainties in its J-factor. Ursa Minor was excluded from HAWC’s contribution to the
 605 combination because the source extension model extended Ursa Minor beyond HAWC’s field of
 606 view. Ursa Minor was not expected to contribute significantly to the combined limit, so work was
 607 not invested in a solution to include Ursa Minor.

608 The DM annihilation channels probed for the Glory Duck combination include
 609 $b\bar{b}$, $e\bar{e}$, $\mu\bar{\mu}$, $\tau\bar{\tau}$, $t\bar{t}$, W^+W^- , and ZZ . A summary of all sources, with a description of each ex-
 610 periments’ sensitivity to the source, is provided in Table 7.2.

611 7.2.3 Likelihood Methods

612 We perform a standard HAWC binned maximum likelihood analysis using f_{hit} bins 1-9. This
 613 analysis was performed using HAL and 3ML, in Python2 [25, 27]. With these tools we compute
 614 the max from the likelihood profiles and perform a ratio test to calculate the significance of each
 615 source. This analysis is identical to the previous dSph analysis [26] except the sources are treated
 616 as extended. For the vast majority of our sources, this extension is no greater than 2 degrees. We
 617 calculate the likelihood of each source and model, assuming events are Poisson distributed, with

$$\mathcal{L} = \prod_i \frac{(B_i + S_i)^{N_i} e^{-(B_i + S_i)}}{N_i!} \quad (7.2)$$

618 S_i is the sum of expected number of signal counts. B_i is the number of background counts
 619 observed. N_i is the total number of counts. The i th bin is iterated over spatial and f_{hit} . Then we
 620 combine the profiles across all five experiments. The profile likelihood ratio λ as a function of
 621 annihilation cross-section $\langle\sigma v\rangle$ is computed by:

$$\lambda(\langle\sigma v\rangle | \mathcal{D}_{\text{dSphs}}) = \frac{\mathcal{L}(\langle\sigma v\rangle; \hat{\nu} | \mathcal{D}_{\text{dSphs}})}{\mathcal{L}(\widehat{\langle\sigma v\rangle}; \hat{\nu} | \mathcal{D}_{\text{dSphs}})} \quad (7.3)$$

622 for a considered annihilation channel and DM mass.

623 **TODO: Section pasted from paper. Rephrase cause plagiarism is a thing.** As mentioned pre-
 624 viously, each experiment computes the \mathcal{L}_{lk} from Equation (7.3) differently. The remainder of

Table 7.1 Summary of the relevant properties of the dSphs used in the present work. Column 1 lists the dSphs. Columns 2 and 3 present their heliocentric distance and galactic coordinates, respectively. Columns 4 and 5 report the J -factors of each source given from the \mathcal{GS} and \mathcal{B} independent studies and their estimated $\pm 1\sigma$ uncertainties. The values $\log_{10} J$ (\mathcal{GS} set) [30] correspond to the mean J -factor values for a source extension truncated at the outermost observed star. The values $\log_{10} J$ (\mathcal{B} set) [31] are provided for a source extension at the tidal radius of each dSph. **Bolded sources are within HAWC's field of view and provided to the Glory Duck analysis.**

| Name | Distance (kpc) | l, b ($^{\circ}$) | $\log_{10} J$ (\mathcal{GS} set) $\log_{10}(\text{GeV}^2\text{cm}^{-5}\text{sr})$ | $\log_{10} J$ (\mathcal{B} set) $\log_{10}(\text{GeV}^2\text{cm}^{-5}\text{sr})$ |
|--------------------------|-------------------|--------------------------|---|--|
| Boötes I | 66 | 358.08, 69.62 | $18.24^{+0.40}_{-0.37}$ | $18.85^{+1.10}_{-0.61}$ |
| Canes Venatici I | 218 | 74.31, 79.82 | $17.44^{+0.37}_{-0.28}$ | $17.63^{+0.50}_{-0.20}$ |
| Canes Venatici II | 160 | 113.58, 82.70 | $17.65^{+0.45}_{-0.43}$ | $18.67^{+1.54}_{-0.97}$ |
| Carina | 105 | 260.11, -22.22 | $17.92^{+0.19}_{-0.11}$ | $18.02^{+0.36}_{-0.15}$ |
| Coma Berenices | 44 | 241.89, 83.61 | $19.02^{+0.37}_{-0.41}$ | $20.13^{+1.56}_{-1.08}$ |
| Draco | 76 | 86.37, 34.72 | $19.05^{+0.22}_{-0.21}$ | $19.42^{+0.92}_{-0.47}$ |
| Fornax | 147 | 237.10, -65.65 | $17.84^{+0.11}_{-0.06}$ | $17.85^{+0.11}_{-0.08}$ |
| Hercules | 132 | 28.73, 36.87 | $16.86^{+0.74}_{-0.68}$ | $17.70^{+1.08}_{-0.73}$ |
| Leo I | 254 | 225.99, 49.11 | $17.84^{+0.20}_{-0.16}$ | $17.93^{+0.65}_{-0.25}$ |
| Leo II | 233 | 220.17, 67.23 | $17.97^{+0.20}_{-0.18}$ | $18.11^{+0.71}_{-0.25}$ |
| Leo IV | 154 | 265.44, 56.51 | $16.32^{+1.06}_{-1.70}$ | $16.36^{+1.44}_{-1.65}$ |
| Leo V | 178 | 261.86, 58.54 | $16.37^{+0.94}_{-0.87}$ | $16.30^{+1.33}_{-1.16}$ |
| Leo T | 417 | 214.85, 43.66 | $17.11^{+0.44}_{-0.39}$ | $17.67^{+1.01}_{-0.56}$ |
| Sculptor | 86 | 287.53, -83.16 | $18.57^{+0.07}_{-0.05}$ | $18.63^{+0.14}_{-0.08}$ |
| Segue I | 23 | 220.48, 50.43 | $19.36^{+0.32}_{-0.35}$ | $17.52^{+2.54}_{-2.65}$ |
| Segue II | 35 | 149.43, -38.14 | $16.21^{+1.06}_{-0.98}$ | $19.50^{+1.82}_{-1.48}$ |
| Sextans | 86 | 243.50, 42.27 | $17.92^{+0.35}_{-0.29}$ | $18.04^{+0.50}_{-0.28}$ |
| Ursa Major I | 97 | 159.43, 54.41 | $17.87^{+0.56}_{-0.33}$ | $18.84^{+0.97}_{-0.43}$ |
| Ursa Major II | 32 | 152.46, 37.44 | $19.42^{+0.44}_{-0.42}$ | $20.60^{+1.46}_{-0.95}$ |
| Ursa Minor | 76 | 104.97, 44.80 | $18.95^{+0.26}_{-0.18}$ | $19.08^{+0.21}_{-0.13}$ |

Table 7.2 Summary of dSph observations by each experiment used in this work. A ‘-’ indicates the experiment did not observe the dSph for this study. For Fermi-LAT, the exposure at 1 GeV is given. For HAWC, $|\Delta\theta|$ is the absolute difference between the source declination and HAWC latitude. HAWC is more sensitive to sources with smaller $|\Delta\theta|$. For IACTs, we show the zenith angle range, the total exposure, the energy range, the angular radius θ of the signal or ON region, the ratio of exposures between the background-control (OFF) and signal (ON) regions (τ), and the significance of gamma-ray excess in standard deviations, σ .

| Source name | Fermi-LAT | HAWC | H.E.S.S, MAGIC, VERITAS | | | | | | |
|-------------------|---------------------------------|----------------------|-------------------------|------------|--------------|--------------------|--------------|--------|------------------|
| | Exposure (10^{11} s m 2) | $ \Delta\theta $ (°) | IACT | Zenith (°) | Exposure (h) | Energy range (GeV) | θ (°) | τ | S (σ) |
| Boötes I | 2.6 | 4.5 | VERITAS | 15 – 30 | 14.0 | 100–41000 | 0.10 | 8.6 | -1.0 |
| Canes Venatici I | 2.9 | 14.6 | – | – | – | – | – | – | – |
| Canes Venatici II | 2.9 | 15.3 | – | – | – | – | – | – | – |
| Carina | 3.1 | – | H.E.S.S. | 27 – 46 | 23.7 | 310 – 70000 | 0.10 | 18.0 | -0.3 |
| Coma Berenices | 2.7 | 4.9 | H.E.S.S. | 47 – 49 | 11.4 | 550 – 70000 | 0.10 | 14.4 | -0.4 |
| | | | MAGIC | 5 – 37 | 49.5 | 60 – 10000 | 0.17 | 1.0 | – |
| | | | MAGIC | 29 – 45 | 52.1 | 70 – 10000 | 0.22 | 1.0 | – |
| Draco | 3.8 | 38.1 | VERITAS | 25 – 40 | 49.8 | 120 – 70000 | 0.10 | 9.0 | -1.0 |
| Fornax | 2.7 | – | H.E.S.S. | 11 – 25 | 6.8 | 230 – 70000 | 0.10 | 45.5 | -1.5 |
| Hercules | 2.8 | 6.3 | – | – | – | – | – | – | – |
| Leo I | 2.5 | 6.7 | – | – | – | – | – | – | – |
| Leo II | 2.6 | 3.1 | – | – | – | – | – | – | – |
| Leo IV | 2.4 | 19.5 | – | – | – | – | – | – | – |
| Leo V | 2.4 | – | – | – | – | – | – | – | – |
| Leo T | 2.6 | – | – | – | – | – | – | – | – |
| Sculptor | 2.7 | – | H.E.S.S. | 10 – 46 | 11.8 | 200 – 70000 | 0.10 | 19.8 | -2.2 |
| Segue I | 2.5 | 2.9 | MAGIC | 13 – 37 | 158.0 | 60 – 10000 | 0.12 | 1.0 | -0.5 |
| | | | VERITAS | 15 – 35 | 92.0 | 80 – 50000 | 0.10 | 7.6 | 0.7 |
| Segue II | 2.7 | – | – | – | – | – | – | – | – |
| Sextans | 2.4 | 20.6 | – | – | – | – | – | – | – |
| Ursa Major I | 3.4 | 32.9 | – | – | – | – | – | – | – |
| Ursa Major II | 4.0 | 44.1 | MAGIC | 35 – 45 | 94.8 | 120 – 10000 | 0.30 | 1.0 | -2.1 |
| Ursa Minor | 4.1 | – | VERITAS | 35 – 45 | 60.4 | 160 – 93000 | 0.10 | 8.4 | -0.1 |

625 this section highlights the differences in this calculation across the experiments. Four experiments,
 626 namely *Fermi*-LAT, H.E.S.S., HAWC and MAGIC, use a binned likelihood to compute the \mathcal{L}_{lk} . For
 627 these experiments, for each observation \mathcal{D}_{lk} of a given dSph l carried out using a given gamma-ray
 628 detector k , the binned likelihood function is:

$$\mathcal{L}_{lk}(\langle\sigma v\rangle; J_l, \nu_{lk} | \mathcal{D}_{lk}) = \prod_{i=1}^{N_E} \prod_{j=1}^{N_P} \left[\mathcal{P}(s_{lk,ij}(\langle\sigma v\rangle, J_l, \nu_{lk}) + b_{lk,ij}(\nu_{lk} | N_{lk,ij})) \right] \times \mathcal{L}_{lk,\nu}(\nu_{lk} | \mathcal{D}_{\nu_{lk}}) \quad (7.4)$$

630 where N_E and N_P are the number of considered bins in reconstructed energy and arrival
 631 direction, respectively; \mathcal{P} represents a Poisson PDF for the number of gamma-ray candidate events
 632 $N_{lk,ij}$ observed in the i -th bin in energy and j -th bin in arrival direction, when the expected number
 633 is the sum of the expected mean number of signal events s_{ij} (produced by DM annihilation) and of
 634 background events b_{ij} ; $\mathcal{L}_{lk,\nu}$ is the likelihood term for the extra ν_{lk} nuisance parameters that vary
 635 from one instrument k to another. The expected counts for signal events s_{ij} for a given dSph l and
 636 detector k is given by:

$$s_{ij}(\langle\sigma v\rangle, J) = \int_{E'_{\min,i}}^{E'_{\max,i}} dE' \int_{P'_{\min,j}}^{P'_{\max,j}} d\Omega' \int_0^\infty dE \int_{\Delta\Omega_{tot}} d\Omega \int_0^{T_{\text{obs}}} dt \frac{d^2\Phi(\langle\sigma v\rangle, J)}{dEd\Omega} \text{IRF}(E', P' | E, P, t) \quad (7.5)$$

637 where E' and E are the reconstructed and true energies, P' and P the reconstructed and true
 638 arrival directions; $E'_{\min,i}$, $P'_{\min,j}$, $E'_{\max,i}$, and $P'_{\max,j}$ are their lower and upper limits of the i -th
 639 energy bin and the j -th arrival direction bin; T_{obs} is the (dead-time corrected) total observation
 640 time; t is the time along the observations; $d^2\Phi/dEd\Omega$ is the DM flux in the source region (see
 641 Equation (7.1)); and $\text{IRF}(E', P' | E, P, t)$ is the IRF, which can be factorized as the product of the
 642 effective collection area of the detector $A_{\text{eff}}(E, P, t)$, the PDFs for the energy estimator $f_E(E' | E, t)$,
 643 and arrival direction $f_P(P' | E, P, t)$ estimators. Note that for Fermi-LAT, HAWC, MAGIC, and
 644 VERITAS the effect of the finite angular resolution is taken into account through the convolution
 645 of $d\Phi/dEd\Omega$ with f_P in Equation (7.5), whereas in the cases of H.E.S.S. f_P is approximated by a
 646 delta function. This approximation has been made in order to maintain compatibility of the result
 647 with what has been previously published. The difference introduced by this approximation is $< 5\%$

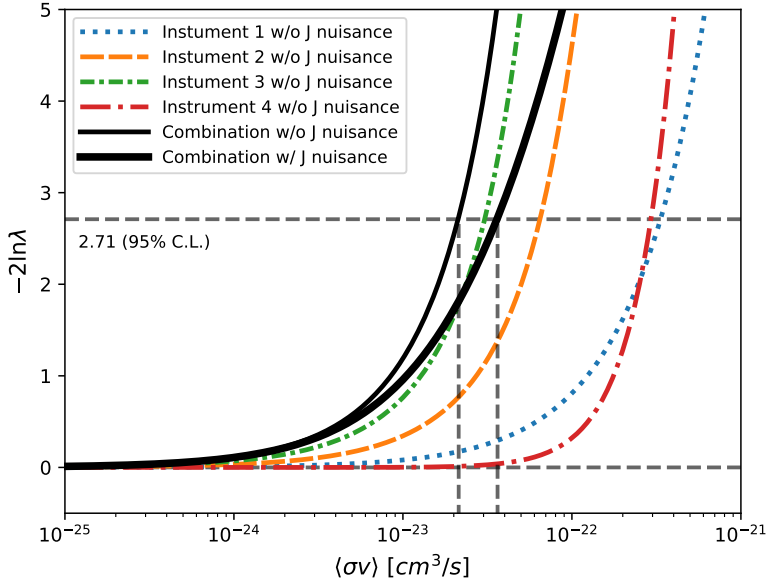


Figure 7.1 Illustration of the combination technique showing a comparison between $-2 \ln \lambda$ provided by four instruments (colored lines) from the observation of the same dSph without any J nuisance and their sum, *i.e.* the resulting combined likelihood (thin black line). According to the test statistics of Equation (7.6), the intersection of the likelihood profiles with the line $-2 \ln \lambda = 2.71$ indicates the 95% C.L. upper limit on $\langle \sigma v \rangle$. The combined likelihood (thin black line) shows a smaller value of upper limit on $\langle \sigma v \rangle$ than those derived by individual instruments. We also show the uncertainties on the J -factor affects the combined likelihood and degrade the upper limit on $\langle \sigma v \rangle$ (thick black line). All likelihood profiles are normalized so that the global minimum $\widehat{\langle \sigma v \rangle}$ is 0. We note that each profile depends on the observational conditions in which a target object was observed. The sensitivity of a given instrument can be degraded and the upper limits less constraining if the observations are performed in non optimal conditions such as a high zenith angle or a short exposure time.

648 for all considered dSphs. **TODO: End of paper section**

649 From Equation (7.3), we can compute the test statistic (TS) with the ratio test:

$$TS = -2 \ln \left(\frac{\mathcal{L}}{\mathcal{L}^{\max}} \right). \quad (7.6)$$

650 \mathcal{L}^{\max} here is equivalent to $\mathcal{L}(N_i, B_i, S_i = 0)$ or no signal counts.

651 7.3 HAWC Results

652 13 of the 20 dSphs considered for the Glory Duck analysis are within HAWC's field of view.

653 These dSph are analyzed for DM content according to the likelihood method described in Sec-

654 tion 7.2.3. The 13 likelihood profiles are then combined to create a combined limit on the dark
655 matter cross-section. This combination is done for 7 of the 8 annihilation channels used in the Glory
656 Duck analysis. Figure 7.2 shows the combined limit for all annihilation channels with HAWC only
657 observations. We also perform 300 studies of Poisson trials on the background. These trials are
658 used to produce HAWC Brazil bands are shared with the other collaborators for combined Brazil
659 Bands. The results on fitting to HAWC’s poisson trials of the DM hypothesis is shown in Figure 7.3
660 for seven of the DM annihilation channels.

661 No DM was found in HAWC observations. The limits are dominated by the dSph Segue1 and
662 Coma Berenices. The remaining 11 dSphs do no contribute significantly to the limit. Even though
663 the remaining dSphs have large J-factors, they are towards the edge of HAWC’s field of view where
664 this analysis is less sensitive.

665 7.4 Glory Duck Combined Results

666 The crux of this analysis is that HAWC’s results are combined with 4 other gamma-ray obser-
667 vatories: Fermi-LAT, H.E.S.S., MAGIC, and VERITAS. The complete joint likelihood for the l -th
668 dSph is the product of likelihood functions of the 5 experiments.

669 **TODO: place holder for results**

670 No significant DM emission was observed by any of the five telescopes. We present upper
671 limits on $\langle\sigma v\rangle$ using the test statistics, Eq. (7.6).

$$TS = -2 \ln \lambda(\langle\sigma v\rangle), \quad (7.7)$$

672 No significant DM emission was observed by any of the five instruments. We present the upper
673 limits on $\langle\sigma v\rangle$ assuming seven independent DM self annihilation channels, namely W^+W^- , Z^+Z^- ,
674 $b\bar{b}$, $t\bar{t}$, e^+e^- , $\mu^+\mu^-$, and $\tau^+\tau^-$. The 68% and 95% containment bands are produced from 300
675 Poisson realizations of the null hypothesis corresponding to each of the combined datasets. These
676 300 realizations are combined identically to dSph observations. The containment bands and the
677 median are extracted from the distribution of resulting limits on the null hypothesis. These 300
678 realizations are obtained either by fast simulations of the OFF observations, for H.E.S.S., MAGIC,

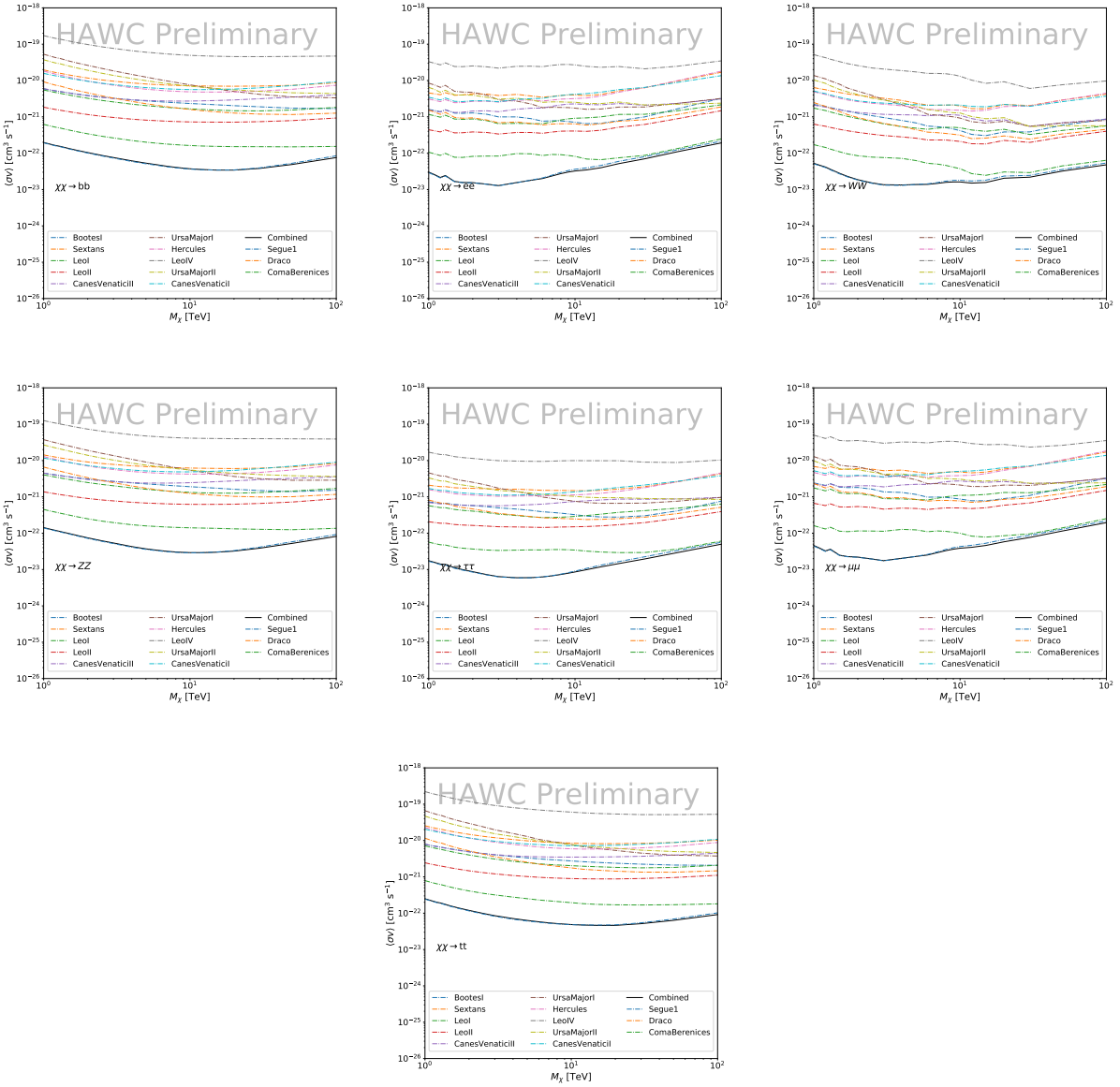


Figure 7.2 HAWC upper limits at 95% confidence level on $\langle\sigma v\rangle$ versus DM mass for seven annihilation channels, using the set of J -factors from Ref. [29]. The solid line represents the observed combined limit. Dashed lines represent limits from individual dSphs.

679 VERITAS, and HAWC, or taken from real observations of empty fields of view in the case of
 680 Fermi-LAT [32, 33, 34].

681 The obtained limits are shown in Figure 7.4 for the $\mathcal{G}\mathcal{S}$ set of J -factors [29] and in Figure 7.5
 682 for the \mathcal{B} set of J -factors [31, 35]. The combined limits are presented with their 68% and 95%
 683 containment bands, and are expected to be close to the median limit when no signal is present.

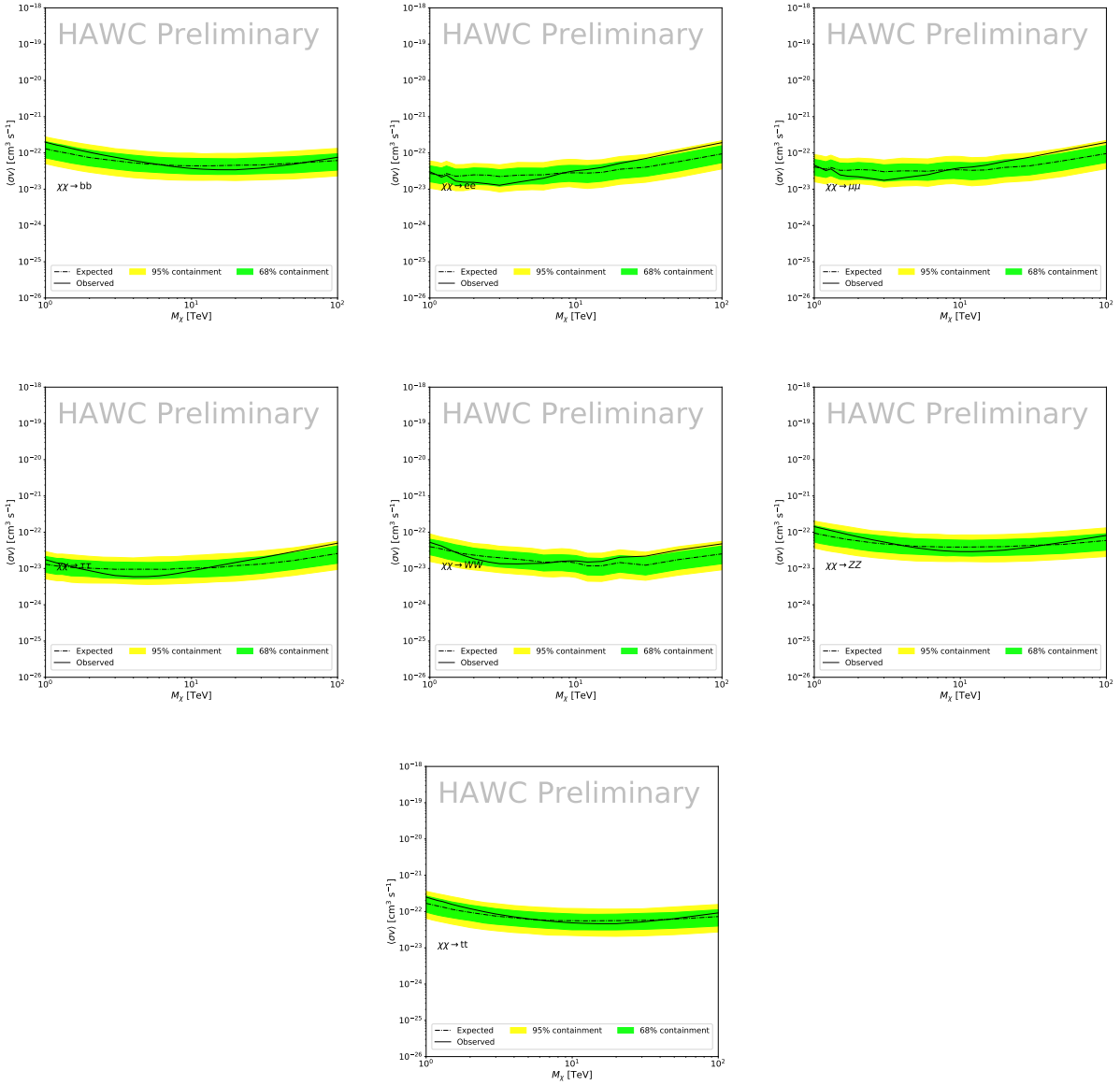


Figure 7.3 HAWC Brazil bands at 95% confidence level on $\langle\sigma v\rangle$ versus DM mass for seven annihilation channels with J -factors from \mathcal{GS} [29]. The solid line represents the combined limit from 13 dSphs. The dashed line is the expected limit. The green band is the 68% containment. The yellow band is the 95% containment.

We observe agreement with the null hypothesis for all channels, within 2σ standard deviations, between the observed limits and the expectations given by the median limits. Limits obtained from each detector are also indicated in the figures, where limits for all dSphs observed by the specific instrument have been combined.

Below ~ 300 GeV, the *Fermi*-LAT dominates the DM limits for all annihilation channels. From

689 ~300 GeV to ~2 TeV, *Fermi*-LAT continues to dominate for the hadronic and bosonic DM channels,
690 yet the IACTs (H.E.S.S., MAGIC, and VERITAS) and *Fermi*-LAT all contribute to the limit for
691 leptonic DM channels. For DM masses between ~2 TeV to ~10 TeV, the IACTs dominate leptonic
692 DM annihilation channels, whereas both the *Fermi*-LAT and the IACTs dominate bosonic and
693 hadronic DM annihilation channels. From ~10 TeV to ~100 TeV, both the IACTs and HAWC
694 contribute significantly to the leptonic DM limit. For hadronic and bosonic DM, the IACTs and
695 *Fermi*-LAT both contribute strongly.

696 We notice that the limits computed using the \mathcal{B} set of J -factor are always better compared to the
697 ones calculated with the \mathcal{GS} set. For the W^+W^- , Z^+Z^- , $b\bar{b}$, and $t\bar{t}$ channels, the ratio between the
698 limits computed with the two sets of J -factor is varying between a factor of ~3 and ~5 depending on
699 the energy, with the largest ratio around 10 TeV. For the channels e^+e^- , $\mu^+\mu^-$, and $\tau^+\tau^-$, the ratio
700 lies between ~2 to ~6, being maximum around 1 TeV. Examining **????** in **??**, these differences are
701 explained by the fact that the \mathcal{B} set provides higher J -factors for the majority of the studied dSphs,
702 with the notable exception of Segue I. The variation on the ratio of the limits for the two sets is due
703 to different dSph dominating the limits depending on the energy. This pushes the range of thermal
704 cross-section which can be excluded to higher mass. This comparison demonstrates the magnitude
705 of systematic uncertainties associated with the choice of the J -factor

706 This comparison demonstrates the magnitude of systematic uncertainties associated with the
707 choice of the J -factor calculation. The \mathcal{GS} and \mathcal{B} sets present a difference in the limits for all
708 channels of about This difference is explained, see **????** in Appendix, by the fact that the \mathcal{B}
709 set provides higher J factors for all dSph except for Segue I. This pushes the range of thermal
710 cross-section which can be excluded to higher mass.

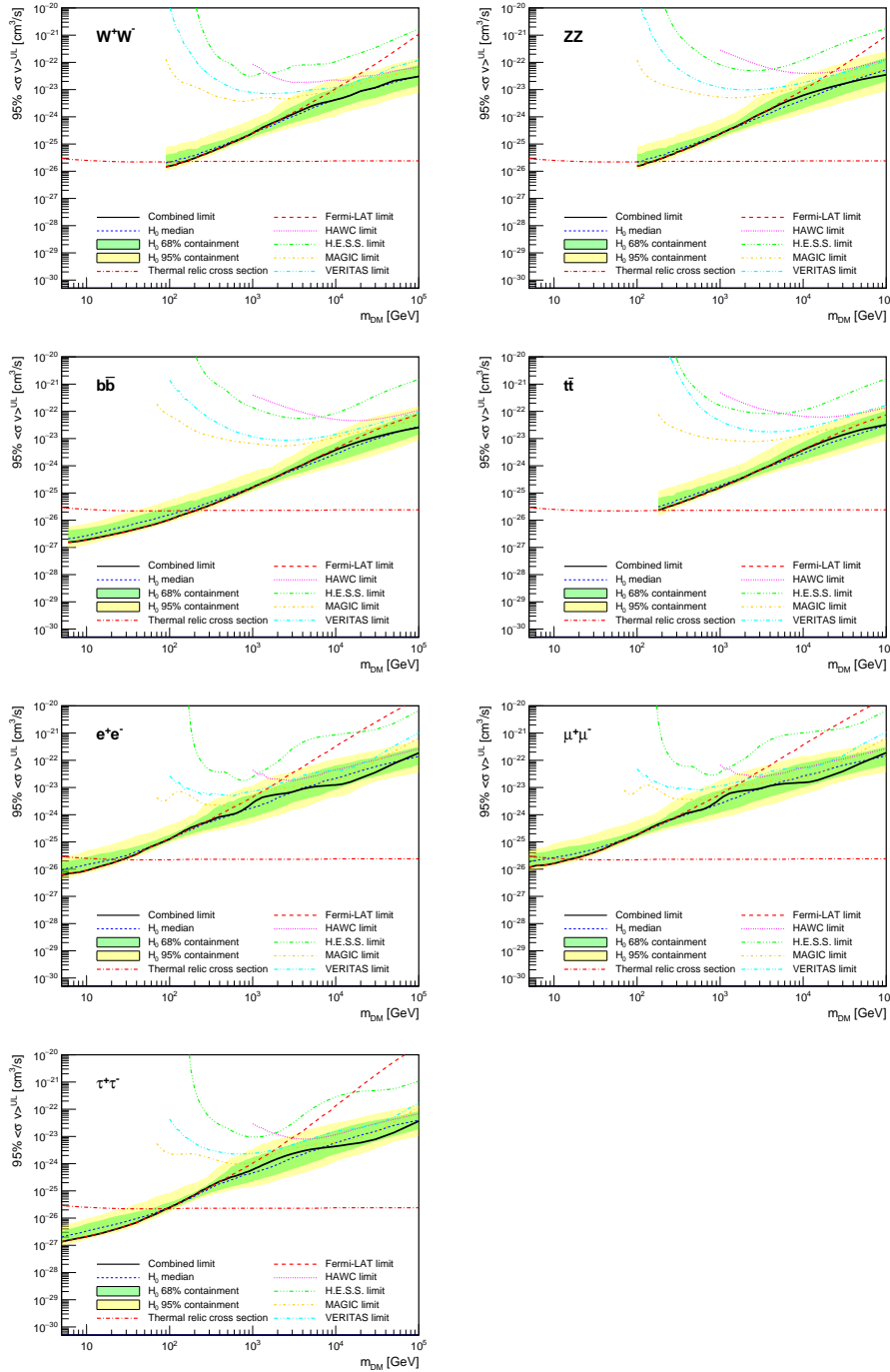


Figure 7.4 Upper limits at 95% confidence level on $\langle\sigma v\rangle$ in function of the DM mass for eight annihilation channels, using the set of J factors from Ref. [29] (\mathcal{GS} set in Table 7.1). The black solid line represents the observed combined limit, the black dashed line is the median of the null hypothesis corresponding to the expected limit, while the green and yellow bands show the 68% and 95% containment bands. Combined upper limits for each individual detector are also indicated as solid, colored lines. The value of the thermal relic cross-section in function of the DM mass is given as the red dotted-dashed line [36].

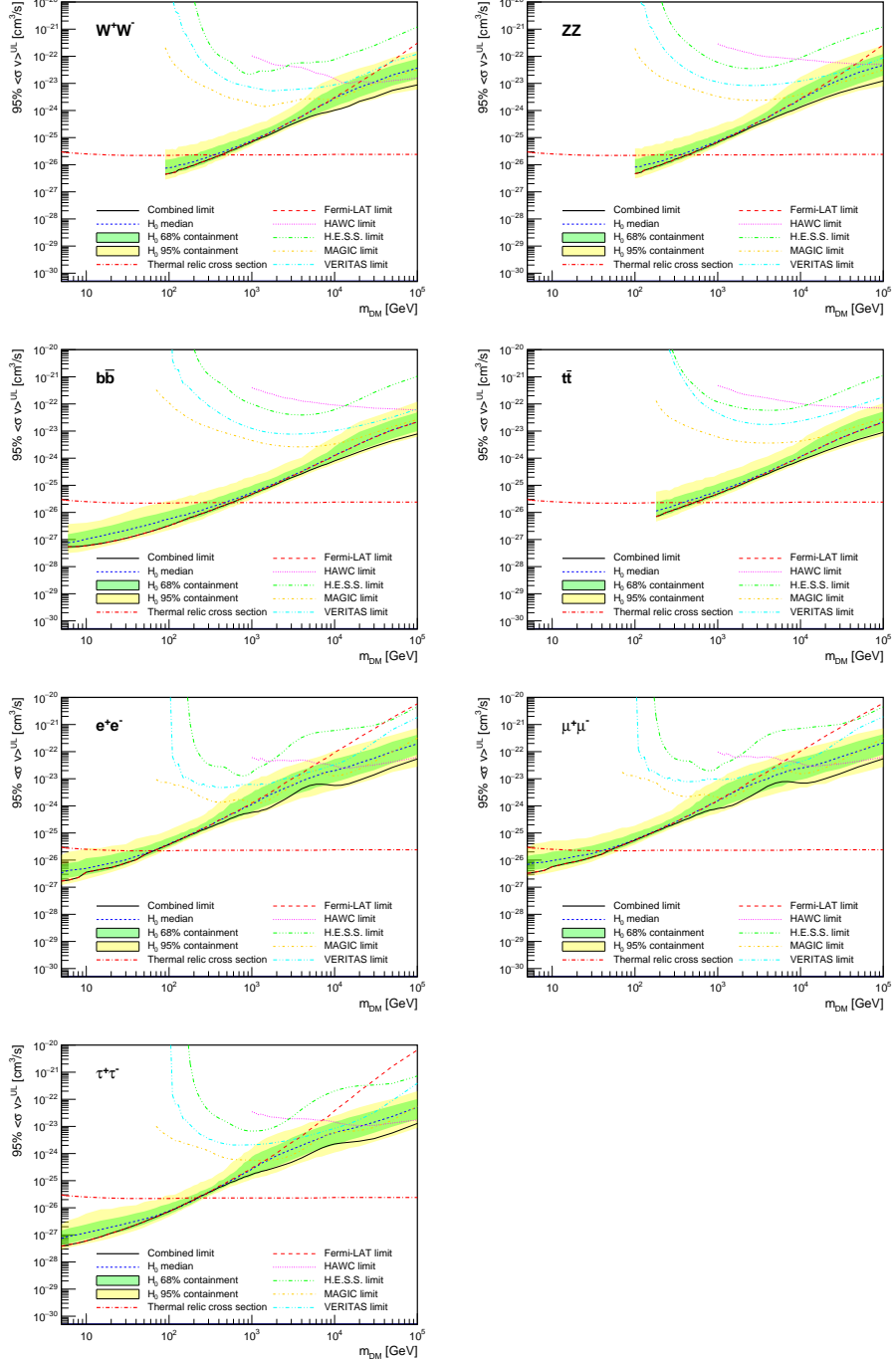


Figure 7.5 Same as Fig. 7.4, using the set of J factors from Ref. [31, 35] (\mathcal{B} set in Table 7.1).

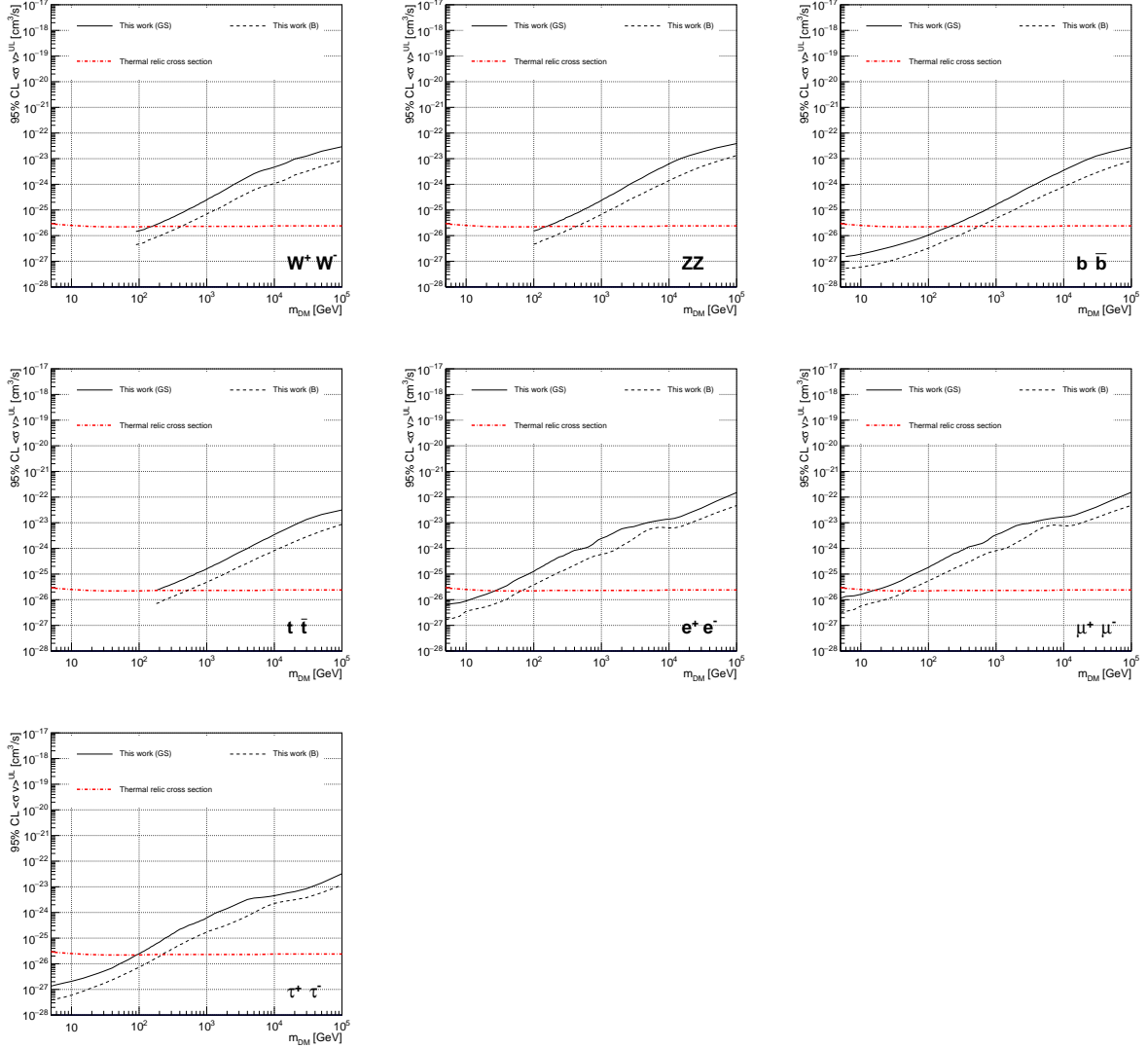


Figure 7.6 Comparisons of the combined limits at 95% confidence level for each of the eight annihilation channels when using the J factors from Ref. [29] (\mathcal{GS} set in Table 7.1), plain lines, and the J factor from Ref. [31, 35] (\mathcal{B} set in Table 7.1), dashed lines. The cross-section given by the thermal relic is also indicated [36].

CHAPTER 8

NU DUCK

711

BIBLIOGRAPHY

- 713 [1] Anne M. Green. “Dark matter in astrophysics/cosmology”. In: *SciPost Phys. Lect.*
 714 *Notes* (2022), p. 37. doi: [10.21468/SciPostPhysLectNotes.37](https://doi.org/10.21468/SciPostPhysLectNotes.37). URL: <https://scipost.org/10.21468/SciPostPhysLectNotes.37>.
- 716 [2] Bing-Lin Young. “A survey of dark matter and related topics in cosmology”. In: *Frontiers*
 717 *of Physics* 12 (Oct. 2016). doi: <https://doi.org/10.1007/s11467-016-0583-4>.
 718 URL: <https://doi.org/10.1007/s11467-016-0583-4>.
- 719 [3] Gianfranco Bertone, Dan Hooper, and Joseph Silk. “Particle dark matter: evidence,
 720 candidates and constraints”. In: *Physics Reports* 405.5 (2005), pp. 279–390. ISSN:
 721 0370-1573. doi: <https://doi.org/10.1016/j.physrep.2004.08.031>. URL:
 722 <https://www.sciencedirect.com/science/article/pii/S0370157304003515>.
- 723 [4] Gianfranco Bertone and Dan Hooper. “History of dark matter”. In: *Rev. Mod. Phys.*
 724 90 (4 Aug. 2018), p. 045002. doi: [10.1103/RevModPhys.90.045002](https://doi.org/10.1103/RevModPhys.90.045002). URL: <https://link.aps.org/doi/10.1103/RevModPhys.90.045002>.
- 726 [5] Fritz Zwicky. “The Redshift of Extragalactic Nebulae”. In: *Helvetica Physica Acta* 6.
 727 (1933), pp. 110–127. doi: [10.5169/seals-110267](https://doi.org/10.5169/seals-110267).
- 728 [6] Vera C. Rubin and Jr. Ford W. Kent. “Rotation of the Andromeda Nebula from a
 729 Spectroscopic Survey of Emission Regions”. In: *ApJ* 159 (Feb. 1970), p. 379. doi:
 730 [10.1086/150317](https://doi.org/10.1086/150317).
- 731 [7] K. G. Begeman, A. H. Broeils, and R. H. Sanders. “Extended rotation curves of spiral galaxies: dark haloes and modified dynamics”. In: *Monthly Notices of the Royal Astronomical Society* 249.3 (Apr. 1991), pp. 523–537. ISSN: 0035-8711. doi: [10.1093/mnras/249.3.523](https://doi.org/10.1093/mnras/249.3.523). eprint: <https://academic.oup.com/mnras/article-pdf/249/3/523/18160929/mnras249-0523.pdf>. URL: <https://doi.org/10.1093/mnras/249.3.523>.
- 736 [8] *Different types of gravitational lenses*. website. Feb. 2004. URL: <https://esahubble.org/images/heic0404b/>.
- 738 [9] Douglas Clowe et al. “A Direct Empirical Proof of the Existence of Dark Matter”. In: *apjl*
 739 648.2 (Sept. 2006), pp. L109–L113. doi: [10.1086/508162](https://doi.org/10.1086/508162). arXiv: [astro-ph/0608407](https://arxiv.org/abs/astro-ph/0608407)
 740 [[astro-ph](#)].
- 741 [10] Planck Collaboration and N. et. al. Aghanim. “Planck 2018 results I. Overview and the
 742 cosmological legacy of Planck”. In: *A&A* 641 (2020). doi: [10.1051/0004-6361/201833880](https://doi.org/10.1051/0004-6361/201833880). URL: <https://doi.org/10.1051/0004-6361/201833880>.
- 744 [11] Wayne Hu. *Matter Density Animation*. web. 2024. URL: <http://background.uchicago.edu/~whu/animbut/anim2.html>.

- 746 [12] Wenlong Yuan et al. “A First Look at Cepheids in a Type Ia Supernova Host with JWST”. in:
747 *The Astrophysical Journal Letters* 940.1 (Nov. 2022). doi: [10.3847/2041-8213/ac9b27](https://doi.org/10.3847/2041-8213/ac9b27).
748 URL: <https://dx.doi.org/10.3847/2041-8213/ac9b27>.
- 749 [13] Wendy L. Freedman. “Measurements of the Hubble Constant: Tensions in Perspective”. In:
750 *The Astrophysical Journal* 919.1 (Sept. 2021), p. 16. doi: [10.3847/1538-4357/ac0e95](https://doi.org/10.3847/1538-4357/ac0e95).
751 URL: <https://dx.doi.org/10.3847/1538-4357/ac0e95>.
- 752 [14] Jodi Cooley. “Dark Matter direct detection of classical WIMPs”. In: *SciPost Phys. Lect.
753 Notes* (2022), p. 55. doi: [10.21468/SciPostPhysLectNotes.55](https://doi.org/10.21468/SciPostPhysLectNotes.55). URL: <https://scipost.org/10.21468/SciPostPhysLectNotes.55>.
- 755 [15] “Search for new phenomena in events with an energetic jet and missing transverse momentum
756 in pp collisions at $\sqrt{s} = 13$ TeV with the ATLAS detector”. In: *Phys. Rev. D* 103
757 (11 July 2021), p. 112006. doi: [10.1103/PhysRevD.103.112006](https://doi.org/10.1103/PhysRevD.103.112006). URL: <https://link.aps.org/doi/10.1103/PhysRevD.103.112006>.
- 759 [16] *Jetting into the dark side: a precision search for dark matter*. website. July 2020. URL:
760 <https://atlas.cern/updates/briefing/precision-search-dark-matter>.
- 761 [17] Celine Armand et. al. “Combined dark matter searches towards dwarf spheroidal galaxies
762 with Fermi-LAT, HAWC, H.E.S.S., MAGIC, and VERITAS”. in: *Proceedings of Science*.
763 Vol. 395. Mar. 2022. doi: <https://doi.org/10.22323/1.395.0528>.
- 764 [18] Tracy R. Slatyer. “Les Houches Lectures on Indirect Detection of Dark Matter”. In: *SciPost
765 Phys. Lect. Notes* (2022), p. 53. doi: [10.21468/SciPostPhysLectNotes.53](https://doi.org/10.21468/SciPostPhysLectNotes.53). URL:
766 <https://scipost.org/10.21468/SciPostPhysLectNotes.53>.
- 767 [19] Christian W Bauer, Nicholas L. Rodd, and Bryan R. Webber. “Dark matter spectra from
768 the electroweak to the Planck scale”. In: *Journal of High Energy Physics* 2021.1029-8479
769 (June 2021). doi: [https://doi.org/10.1007/JHEP06\(2021\)121](https://doi.org/10.1007/JHEP06(2021)121).
- 770 [20] Riccardo Catena and Piero Ullio. “A novel determination of the local dark matter density”.
771 In: *Journal of Cosmology and Astroparticle Physics* 2010.08 (Aug. 2010), p. 004. doi:
772 [10.1088/1475-7516/2010/08/004](https://doi.org/10.1088/1475-7516/2010/08/004). URL: <https://dx.doi.org/10.1088/1475-7516/2010/08/004>.
- 774 [21] B. P. Abbott et al. “Observation of Gravitational Waves from a Binary Black Hole Merger”.
775 In: *Phys. Rev. Lett.* 116 (6 Feb. 2016), p. 061102. doi: [10.1103/PhysRevLett.116.061102](https://doi.org/10.1103/PhysRevLett.116.061102). URL: <https://link.aps.org/doi/10.1103/PhysRevLett.116.061102>.
- 777 [22] R. Abbasi et. al. “Observation of high-energy neutrinos from the Galactic plane”. In: *Science*
778 380.6652 (June 2023), pp. 1338–1343.
- 779 [23] NASA Goddard Space Flight Center. *Fermi’s 12-year view of the gamma-ray sky*. website.

- 780 2022. URL: <https://svs.gsfc.nasa.gov/14090>.
- 781 [24] Marco Cirelli et al. “PPPC 4 DM ID: a poor particle physicist cookbook for dark matter
782 indirect detection”. In: *Journal of Cosmology and Astroparticle Physics* 2011.03 (Mar.
783 2011), p. 051. doi: [10.1088/1475-7516/2011/03/051](https://doi.org/10.1088/1475-7516/2011/03/051). URL: <https://dx.doi.org/10.1088/1475-7516/2011/03/051>.
- 785 [25] A. U. Abeysekara et al. “Observation of the Crab Nebula with the HAWC Gamma-Ray
786 Observatory”. In: *The Astrophysical Journal* 843.1 (June 2017), p. 39. doi: [10.3847/1538-4357/aa7555](https://doi.org/10.3847/1538-4357/aa7555). URL: <https://doi.org/10.3847/1538-4357/aa7555>.
- 788 [26] A. Albert et al. “Dark Matter Limits from Dwarf Spheroidal Galaxies with the HAWC
789 Gamma-Ray Observatory”. In: *The Astrophysical Journal* 853.2 (Feb. 2018), p. 154. ISSN:
790 1538-4357. doi: [10.3847/1538-4357/aaa6d8](https://doi.org/10.3847/1538-4357/aaa6d8). URL: [http://dx.doi.org/10.3847/1538-4357/aaa6d8](https://dx.doi.org/10.3847/1538-4357/aaa6d8).
- 792 [27] Giacomo Vianello et al. *The Multi-Mission Maximum Likelihood framework (3ML)*. 2015.
793 arXiv: [1507.08343](https://arxiv.org/abs/1507.08343) [astro-ph.HE].
- 794 [28] Marco Cirelli et al. “PPPC 4 DM ID: a poor particle physicist cookbook for dark matter
795 indirect detection”. In: *Journal of Cosmology and Astroparticle Physics* 2011.03 (Mar.
796 2011). ISSN: 1475-7516. doi: [10.1088/1475-7516/2011/03/051](https://doi.org/10.1088/1475-7516/2011/03/051). URL: [http://dx.doi.org/10.1088/1475-7516/2011/03/051](https://dx.doi.org/10.1088/1475-7516/2011/03/051).
- 798 [29] Alex Geringer-Sameth and Matthew Koushiappas Savvas M. and Walker. “Dwarf galaxy
799 annihilation and decay emission profiles for dark matter experiments”. In: *Astrophys.
800 J.* 801.2 (2015), p. 74. doi: [10.1088/0004-637X/801/2/74](https://doi.org/10.1088/0004-637X/801/2/74). arXiv: [1408.0002](https://arxiv.org/abs/1408.0002)
801 [astro-ph.CO].
- 802 [30] Alex Geringer-Sameth, Savvas M. Koushiappas, and Matthew Walker. “DWARF GALAXY
803 ANNIHILATION AND DECAY EMISSION PROFILES FOR DARK MATTER EXPERI-
804 MENTS”. in: *The Astrophysical Journal* 801.2 (Mar. 2015), p. 74. ISSN: 1538-4357. doi:
805 [10.1088/0004-637x/801/2/74](https://doi.org/10.1088/0004-637x/801/2/74). URL: [http://dx.doi.org/10.1088/0004-637X/801/2/74](https://dx.doi.org/10.1088/0004-637X/801/2/74).
- 807 [31] V. Bonnivard et al. “Spherical Jeans analysis for dark matter indirect detection in dwarf
808 spheroidal galaxies - Impact of physical parameters and triaxiality”. In: *Mon. Not. Roy.
809 Astron. Soc.* 446 (2015), pp. 3002–3021. doi: [10.1093/mnras/stu2296](https://doi.org/10.1093/mnras/stu2296). arXiv:
810 [1407.7822](https://arxiv.org/abs/1407.7822) [astro-ph.HE].
- 811 [32] M. Ackermann et al. “Searching for Dark Matter Annihilation from Milky Way Dwarf
812 Spheroidal Galaxies with Six Years of Fermi Large Area Telescope Data”. In: *prl* 115.23,
813 231301 (Dec. 2015), p. 231301. doi: [10.1103/PhysRevLett.115.231301](https://doi.org/10.1103/PhysRevLett.115.231301). arXiv:
814 [1503.02641](https://arxiv.org/abs/1503.02641) [astro-ph.HE].

- 815 [33] A. et al. Albert. “Searching for Dark Matter Annihilation in Recently Discovered Milky Way
816 Satellites with Fermi-LAT”. in: *Astrophys. J.* 834.2 (2017), p. 110. doi: [10.3847/1538-4357/834/2/110](https://doi.org/10.3847/1538-4357/834/2/110). arXiv: [1611.03184](https://arxiv.org/abs/1611.03184) [astro-ph.HE].
- 818 [34] Mattia Di Mauro and Martin Wolfgang Winkler. “Multimessenger constraints on the dark
819 matter interpretation of the Fermi-LAT Galactic Center excess”. In: *prd* 103.12, 123005
820 (June 2021), p. 123005. doi: [10.1103/PhysRevD.103.123005](https://doi.org/10.1103/PhysRevD.103.123005). arXiv: [2101.11027](https://arxiv.org/abs/2101.11027)
821 [astro-ph.HE].
- 822 [35] V. Bonnivard et al. “Dark matter annihilation and decay in dwarf spheroidal galaxies: The
823 classical and ultrafaint dSphs”. In: *Mon. Not. Roy. Astron. Soc.* 453.1 (2015), pp. 849–867.
824 doi: [10.1093/mnras/stv1601](https://doi.org/10.1093/mnras/stv1601). arXiv: [1504.02048](https://arxiv.org/abs/1504.02048) [astro-ph.HE].
- 825 [36] Gianfranco Bertone, Dan Hooper, and Joseph Silk. “Particle dark matter: evidence, can-
826 didates and constraints”. In: *Physics Reports* 405.5-6 (Jan. 2005), pp. 279–390. ISSN:
827 0370-1573. doi: [10.1016/j.physrep.2004.08.031](https://doi.org/10.1016/j.physrep.2004.08.031). URL: <http://dx.doi.org/10.1016/j.physrep.2004.08.031>.